

Angular Sizes and Effective Temperatures of O-type Stars from Optical Interferometry with the CHARA Array

KATHRYN D. GORDON,¹ DOUGLAS R. GIES,¹ GAIL H. SCHAEFER,² DANIEL HUBER,³ MICHAEL IRELAND,⁴ AND
 D. JOHN HILLIER⁵

¹*Center for High Angular Resolution Astronomy and Department of Physics and Astronomy,
 Georgia State University, P. O. Box 5060, Atlanta, GA 30302-5060, USA*

²*The CHARA Array of Georgia State University, Mount Wilson Observatory, Mount Wilson, CA 91023, USA*

³*Institute for Astronomy, University of Hawai‘i, 2680 Woodlawn Drive, Honolulu, HI 96822, USA*

⁴*Research School of Astronomy & Astrophysics, Australian National University, Canberra, ACT 2611, Australia*

⁵*Department of Physics and Astronomy and Pittsburgh Particle Physics, Astrophysics, and Cosmology Center (PITT PACC),
 University of Pittsburgh, Pittsburgh, PA 15260, USA*

Submitted to AJ

ABSTRACT

We present interferometric observations of six O-type stars that were made with the Precision Astronomical Visible Observations (PAVO) beam combiner at the Center for High Angular Resolution Astronomy (CHARA) Array. The observations include multiple brackets for three targets, λ Ori A, ζ Oph, and 10 Lac, but there are only preliminary, single observations of the other three stars, ξ Per, α Cam, and ζ Ori A. The stellar angular diameters range from 0.55 milliarcsec for ζ Ori A down to 0.11 mas for 10 Lac, the smallest star yet resolved with the CHARA Array. The rotational oblateness of the rapidly rotating star ζ Oph is directly measured for the first time. We assembled ultraviolet to infrared flux measurements for these stars, and then derived angular diameters and reddening estimates using model atmospheres and an effective temperature set by published results from analysis of the line spectrum. The model-based angular diameters are in good agreement with observed angular diameters. We also present estimates for the effective temperatures of these stars derived by setting the interferometric angular size and fitting the spectrophotometry.

Keywords: stars: early-type — stars: fundamental parameters — stars: massive — techniques: interferometric

1. INTRODUCTION

The fundamental properties of **early O-type stars**, such as mass, radius, and temperature, are the essential parameters required to place stars in the Hertzsprung-Russell diagram for comparison with stellar evolutionary tracks. The derivation of these quantities is usually reserved to members of eclipsing binary stars in which combined radial velocity and photometric light curve analysis can yield estimates of mass and radius (Torres et al. 2010). However, some of these systems probably interacted at some point in their evolution, and com-

parisons of their properties with evolutionary tracks for single stars may not be entirely reliable. Instead, most of the work on the fundamental parameters of individual **O-type stars** is based on analysis of the line spectrum, in which the temperature and gravity are derived from the He line ionization balance and the pressure broadening of the hydrogen lines. These studies rely upon detailed atmospheric models that must take into account non-LTE populations, line-blanketing, and spherical winds. FASTWIND (Santolaya-Rey et al. 1997; Puls et al. 2005), TLUSTY (Hubeny & Lanz 1995), and CMFGEN (Hillier & Miller 1998) are all non-LTE models that can be applied to O-star atmospheres and use different methods to deal with the line-blanketing problem. FASTWIND and CMFGEN also take into account the effects of winds (important in more luminous stars)

while TLUSTY does not. These studies are often used to calibrate the MK-classifications of O-stars in terms of temperature and gravity (Martins et al. 2005; Holgado et al. 2018). **However, although these calibrations serve as a general reference to connect the spectral classifications of a given star and their parameters, one has to use them carefully when studying the properties of a specific individual target of interest.** For example, Simón-Díaz et al. (2014) applied spectral line fits using FASTWIND models to investigate the effective temperature relation with O-subtype. They found a significant scatter of effective temperatures among O-stars of similar spectral type that is partially due to the variation of $\log g$ within O-dwarf luminosity class.

It is important to test the atmosphere models for O-stars because we now rely upon them so completely. The simplest approach in principle is to determine the stellar effective temperature T_{eff} from the relationship between the extinction corrected bolometric flux, angular diameter θ , and effective temperature: $f_{\text{bol}} = \frac{1}{4}\theta^2\sigma T_{\text{eff}}^4$. This method was pioneered by Hanbury Brown et al. (1974) who used the Narrabri Stellar Intensity Interferometer (NSII) to measure the angular diameters of 32 stars in the spectral range from O5 to F8 (including two stars considered here). Code et al. (1976) used the early satellite observations of the UV flux of these stars to record their spectral energy distribution (SED) and determine effective temperature. However, there were only three O-type stars in the sample observed by Hanbury Brown et al. (1974), and the great distances of the O-stars made other high angular resolution measurements impossible until now.

Furthermore, there are a number of intrinsic problems in using the flux and angular diameter method that were initially discussed by Abbott & Hummer (1985) and Hummer et al. (1988). The primary issue is that most O-stars radiate a large fraction of their flux in the extreme UV, at wavelengths smaller than the Lyman limit at 912 Å. This part of the spectrum is totally obscured by the local interstellar medium in general, and consequently we must rely upon stellar atmosphere models to predict the flux at short wavelengths. The region of spectrum we can observe is in the Rayleigh-Jeans tail where the continuum shape is more or less independent of temperature, so that the intrinsic shape of the UV continuum (Massa & Savage 1985) and unreddened optical/IR colors (Martins & Plez 2006) are similar among all O-stars. The second problem is that the flux in the observed part of the spectrum has a gravity dependence. The size of the Lyman jump in the SED depends on the ionization state of H, and the higher ratio of ionized to neutral H

atoms among the supergiants results in a smaller Lyman jump and lower flux at longer wavelengths compared to that of the dwarf O-stars with the same T_{eff} (see Fig. 11 in Lanz & Hubeny 2003). Consequently, the star's gravity must be known from other means in order to fit the observed continuum with an appropriate model. Finally, most O-stars are very distant objects and their flux distributions are altered by interstellar extinction. Thus, fits of their observed flux must deal carefully with the details of dust extinction that can vary with our line of sight through the interstellar medium (Fitzpatrick 1999; Maíz Apellániz et al. 2014).

Four decades after the work of Hanbury Brown et al. (1974), we are now able to renew the flux and angular diameter method thanks to the advent of long-baseline optical interferometry. Using measurements made possible with the Center for High Angular Resolution Astronomy (CHARA) Array (ten Brummelaar et al. 2005), we can determine the angular diameters of the brighter O-stars that have good SED measurements available and that have well-established gravities from detailed studies of their line spectra. The angular diameter measurements need to be accurate in order to compare the continuum and line results. The relation between the emitted F_{λ} and observed f_{λ} monochromatic flux is

$$F_{\lambda}(T_{\text{eff}}, \log g, Z) = f_{\lambda} 10^{0.4A_{\lambda}} / (\theta/2)^2$$

where A_{λ} is the extinction (in magnitudes) and θ is the angular diameter (in radians). The monochromatic flux in the Rayleigh-Jeans tail varies with temperature as $F_{\lambda} \propto T_{\text{eff}}$, so for a given observed monochromatic flux and extinction, the derived temperature will vary as $T_{\text{eff}} \propto \theta^{-2}$ and the fractional uncertainty will be $\Delta T_{\text{eff}}/T_{\text{eff}} \approx 2\Delta\theta/\theta$. Thus, accurate, sub-milliarcsecond angular measurements are needed to provide an effective test of the spectral predictions of the current generation of atmospheric models.

Here we present the results of our angular diameter measurements of a sample of six O-type stars. Section 2 discusses the observations, calibration, and reduction methods to obtain the interferometric visibility as a function of baseline and position angle in the sky. In Section 3.1, we show fits of the visibility measurements to obtain a limb darkened angular diameter θ_{LD} , and in Section 3.2 we collect the available spectrophotometry and make fits of the SED as a function of temperature, angular size, and reddening. In Section 4, we gather distance estimates in order to transform the angular diameters into linear radii, and we compare the angular size derived from interferometry with that from model fits of the continuum flux for published values of effective temperature.

Table 1. Parameters of Target Stars

	Star	HD	Spectral	<i>V</i>	<i>B</i> – <i>V</i>	<i>V</i> – <i>K</i>	<i>T</i> _{eff}	<i>log g</i>	<i>V sin i</i>
Identifier	Name	Number	Classification	(mag)	(mag)	(mag)	(kK)	(c.g.s.)	(km s ⁻¹)
<i>a</i>	ξ Per	24912	O7.5 III((n)((f))	4.06	0.02	0.11	34.3 ± 0.8	3.49 ± 0.12	230
<i>b</i>	α Cam	30614	O9 Ia	4.29	0.05	0.05	29.4 ± 1.0	3.03 ± 0.19	113
<i>c</i>	λ Ori A	36861	O8 III((f))	3.47	0.01	-0.56	34.5 ± 0.8	3.64 ± 0.13	59
<i>d</i>	ζ Ori A	37742	O9.2 Ib	1.88	-0.11	-0.44	29.5 ± 1.0	3.25 ± 0.25	124
<i>e</i>	ζ Oph	149757	O9.2 IVnn	2.56	0.02	-0.06	32.1 ± 1.3	3.66 ± 0.13	311
<i>f</i>	10 Lac	214680	O9 V	4.88	-0.21	-0.62	35.5 ± 0.5	3.97 ± 0.08	16

NOTE—Effective temperatures and gravities are average values taken from the sources listed in Table 2. Spectral types from the Galactic O-Star Spectroscopic Survey (Sota et al. 2011). Projected rotational velocities *V sin i* are from Simón-Díaz & Herrero (2014).

Table 2. Literature Properties: *T*_{eff} (kK), *log g* (c.g.s.)

Source	ξ Per	α Cam	λ Ori A	ζ Ori A	ζ Oph	10 Lac	Code
Bouret et al. (2008)	29.5, 3.25	CMFGEN
Herrero et al. (2002)	35.5, 3.95	FASTWIND
Holgado et al. (2018)	...	29.4, 2.90	35.2, 3.50	35.2, 3.90	IACOB-GBAT
Marcolino et al. (2009)	32.0, 3.60	...	TLUSTY
Markova et al. (2004)	34.0, 3.35	31.0, 3.19	33.6, 3.56	FASTWIND
Martins et al. (2012)	29.5, 3.25	CMFGEN
Martins et al. (2015)	34.0, 3.60	29.5, 3.25	35.0, 3.75	...	31.0, 3.60	35.0, 4.05	CMFGEN
Martins et al. (2017)	33.5, 3.50	...	35.0, 3.75	CMFGEN
Mokiem et al. (2005)	32.1, 3.62	36.0, 4.03	FASTWIND
Najarro et al. (2011)	...	28.9, 3.01	34.5, 3.70	CMFGEN
Puls et al. (2006)	35.0, 3.50	29.0, 3.00	33.6, 3.56	FASTWIND
Repolust et al. (2004)	34.0, 3.50	29.0, 2.97	32.0, 3.65	...	FASTWIND
Repolust et al. (2005)	...	29.0, 2.88	33.5, 3.85	...	FASTWIND
Simón-Díaz et al. (2006)	36.0, 3.90	FASTWIND

Table 3. Companions of Target Stars

Star	Separation	Δm_V	<i>T</i> _{eff}	<i>log g</i>	Spectrophotometric	Interferometric
Name	(arcsec)	(mag)	(kK)	(c.g.s.)	Correction	Correction
ξ Per	2.4 ^a	9.8 ^a	N	N
λ Ori A	4.2 ^a	2.3 ^a	25.4 ^b	4.21 ^b	Y	N
ζ Ori A	0.037 ^d	2.2 ^d	26.7 ^c	4.0 ^c	Y	Y
	2.4 ^a	1.9 ^a	31.0 ^e	3.8 ^e	Y	N
10 Lac	3.6 ^a	9.9 ^a	N	N

NOTE—Last two columns indicate if it was necessary (Y = yes, N = no) to make corrections to the spectrophotometric or interferometric fits due to the companions.

a - Turner et al. (2008); *b* - Lyubimkov et al. (2004); *c* - Typical values for a B1 IV star (Hummel et al. 2013); *d* - Hummel et al. (2013); *e* - Typical values for a B0 III star (Hummel et al. 2013).

2. OBSERVATIONS

The stars in our sample consist of six O spectral type stars ranging from O7.5 to O9. There are two supergiants, two giants, one sub-giant and one dwarf. Table 1 lists the parameters of the objects. The effective temperature T_{eff} given in column 8 is the average of the recently published values that are gathered in Table 2. The gravity log g listed in column 9 is likewise the average from those papers noted in Table 2.

Four of the six O stars observed have close companions reported from speckle, adaptive optics, and other studies listed in the Washington Double Star Catalog¹. Parameters of the companions are shown in Table 3. Most of these companions are faint and have separations greater than the interferometric field of view of $1''$, so their flux has no influence on our interferometric data. The exception is the close companion to ζ Ori A that is discussed below. The companions will, however, contribute to the net flux measured in the spectral energy distributions (with the exception of the negligible contributions from the very faint companions of ξ Per and 10 Lac), and we deal with this complication in Section 3.2 below.

Observations of our targets were made using the PAVO beam combiner (Ireland et al. 2008) at the CHARA Array (ten Brummelaar et al. 2005), located at Mount Wilson Observatory in California. The CHARA Array is an optical interferometer composed of six 1 meter telescopes arranged in a Y-shaped configuration. Combinations of the telescopes allow for 15 different usable baselines ranging in length from 34 meters to 331 meters. Combining the longest usable baseline currently available in the world and the operating wavelength range of the PAVO beam combiner (650 - 800 nm), we are able to achieve an extremely high angular resolution for our targets of about 0.2 milli-arcseconds (mas).

The beams from the Array are fed into the PAVO combiner by a set of lenses and mirrors (Ireland et al. 2008; Maestro et al. 2012). The final set are three small movable prisms that guide the beams to the image plane. After being focused in the image plane, the beams pass through a three-hole mask that spatially filters the light (only two beams and two holes are used here). The beams then interfere and produce fringes that are spatially modulated in the pupil plane. Finally, a lenslet array divides the pupil into 16 segments and a prism disperses the fringes in each segment into 23 or more spectral channels. Throughout a night of observing the alignments of the image and pupil plane are checked

for each new target, fringes are found, and adjustments made to optimize the longitudinal dispersion corrector position.

Data for each target were taken using the standard ‘bracket’ method where one bracket is three scans in order of: calibrator - target - calibrator. Observing in brackets allows the visibilities recorded for the target to be properly calibrated and eventually fit to obtain angular diameters. We obtained multiple brackets for λ Ori A, ζ Oph, and 10 Lac, but we were limited to a single bracket with only one calibrator observation for ξ Per, α Cam, and ζ Ori A, because of changing sky conditions over the timespan of the bracket. The results on these latter three targets are preliminary.

Calibrators are chosen to be unresolved, single, slowly rotating stars that are close to the target in brightness and position in the sky. The angular diameters were adopted from the Jean-Marie Mariotti Center (JMMC) Stellar Diameter Catalog (JSDC²) using values from Version 1 (Lafrasse et al. 2010) for most and from Version 2 (Bourges et al. 2014) for the three calibrator stars associated with the 10 Lac observations. The JSDC diameters are listed in Table 4 and are estimated by making a polynomial fit of the differential surface brightness of a star as a function of spectral type (Chelli et al. 2016). The JSDC diameters are generally in good agreement with independent estimates from CADARS (Pasinetti Fracassini et al. 2001) and Swihart et al. (2017) (see Table 4). The exception is the calibrator for ζ Oph, HD 154445, which has a larger size in the JSDC Catalog. The angular diameter of HD 154445 is given as 0.16 mas by CADARS, 0.18 mas by Swihart et al. (2017), and a spectroscopic study by Lyubimkov et al. (2002) implies a diameter of 0.21 mas. These diameter estimates are all significantly smaller than the JSDC value of 0.28 mas, so we adopted the angular diameter found by Swihart et al. (2017) of 0.18 mas for this calibrator.

Observations of our targets with CHARA were accomplished from 2013 November to 2017 June. For all observations only one baseline, or two telescopes, was used at a time. Observing data, including dates, baselines, and calibrated visibilities, are given in Table 5 (given in full in the electronic version). **Column 4 of Table 5 lists the spatial frequency of the observation, or baseline divided by wavelength. Columns 5 and 6 give the positions in the u, v plane of spatial frequency for each observation. Column 8 gives**

¹ <http://ad.usno.navy.mil/wds/>

² <http://www.jmmc.fr/jsdc>

Table 4. Calibrator Stars

Star	Spectral	Target	θ_{LD} (JSDC)	θ_{LD} (CADARS)	θ_{LD} (Swihart)
Name	Class.	ID	(mas)	(mas)	(mas)
HD 27777	B8 V	<i>a</i>	0.172±0.012	0.20	0.175±0.037
HD 29646	A2 V	<i>d</i>	0.199±0.014	...	0.249±0.019
HD 34989	B1 V	<i>c</i>	0.132±0.009	0.10	0.118±0.026
HD 37320	B8 III	<i>c</i>	0.158±0.011	...	0.163±0.035
HD 38831	A0 Vs	<i>b</i>	0.149±0.010	0.17	...
HD 154445	B1 V	<i>e</i>	0.280±0.019	0.16	0.180±0.041
HD 204403	B3 V	<i>f</i>	0.171±0.006	0.17	0.154±0.048
HD 212978	B2 V	<i>f</i>	0.106±0.004	0.10	...
HD 213272	A2 V	<i>f</i>	0.175±0.005	0.16	...

NOTE—Target ID is the star identifier given in Table 1.

the visibility squared and column 9 gives the uncertainty associated with each V^2 measurement.

The data were reduced using the standard data reduction and fitting pipeline written for use with the PAVO instrument (Ireland et al. 2008; Maestro et al. 2012). This pipeline first takes the raw data through a routine that allows for the rejection of bad data frames. This allows the user to make cuts based on S/N values and loss of lock on fringes. The data undergo background subtraction and photon-bias subtraction, with foreground frames, ratio frames, and dark frames taken during a shutter sequence that runs after fringe data are saved. During a foreground frame all shutters are open but fringe tracking is turned off, and during a ratio frame only one shutter is left open at a time. The processed data are then sent through a second routine that calculates the projected baseline vectors for each observation, calibrates the brackets, and outputs the calibrated visibilities. This routine allows the user to define estimates and uncertainties on the calibrator diameters, as well as provide a limb-darkening coefficient for a linear limb-darkening law.

We generally assume spherical symmetry for the targets so that the angular diameter is independent of the

position angle of the baseline projected on the sky. However, ζ Oph is a special case as it is very rapidly rotating with a projected rotational velocity $V \sin i = 348$ km s $^{-1}$, and it will have a rotationally distorted shape. We observed ζ Oph on two nearly orthogonal baselines to obtain a range in (u, v) coverage and to ascertain the angular size at different position angles across the star.

The target ζ Ori A has a close companion with an orbit measured by Hummel et al. (2013), and the predicted angular separation was 33 mas at the time of our observation with a V -band magnitude difference of 2.2 mag. This companion is close enough and bright enough to contribute extra light and a periodic modulation to the observed visibility measurements, which, if not accounted for, will make the fitted angular size incorrect. The companion flux was taken into account in our interferometric and spectrophotometric fitting of the ζ Ori A measurements. Using our knowledge of the position of the companion based on the measured orbit, we computed a binary model to fit the visibilities (see Section 4.1).

Table 5. Calibrated Visibilities

HD	Telescope	$10^{-6}B/\lambda$	u	v	Baseline	V^2	ΔV^2	
Number	MJD	Pair	(rad $^{-1}$)	(arcsec $^{-1}$)	(arcsec $^{-1}$)	(m)		
(1)	(2)	(3)	(4)	(5)	(6)	(7)	(8)	(9)
24912	57340	W1E1	391.03	-1857.16	-380.64	310.28	0.668	0.025
24912	57340	W1E1	394.91	-1875.60	-384.42	310.28	0.674	0.052
24912	57340	W1E1	398.87	-1894.40	-388.28	310.28	0.675	0.035

Table 5 continued

Table 5 (*continued*)

HD	Telescope		$10^{-6}B/\lambda$	u	v	Baseline	V^2	ΔV^2
Number	MJD	Pair	(rad $^{-1}$)	(arcsec $^{-1}$)	(arcsec $^{-1}$)	(m)	(8)	(9)
(1)	(2)	(3)	(4)	(5)	(6)	(7)		
24912	57340	W1E1	402.65	-1912.35	-391.96	310.28	0.666	0.031
24912	57340	W1E1	406.50	-1930.64	-395.70	310.28	0.585	0.024
24912	57340	W1E1	410.21	-1948.25	-399.31	310.28	0.600	0.039
24912	57340	W1E1	413.93	-1965.92	-402.94	310.28	0.662	0.061
24912	57340	W1E1	417.72	-1983.92	-406.62	310.28	0.720	0.057
24912	57340	W1E1	421.58	-2002.25	-410.38	310.28	0.752	0.057
24912	57340	W1E1	425.51	-2020.92	-414.21	310.28	0.672	0.051
24912	57340	W1E1	429.58	-2040.23	-418.17	310.28	0.628	0.048
24912	57340	W1E1	433.42	-2058.47	-421.90	310.28	0.618	0.059
24912	57340	W1E1	437.33	-2077.03	-425.71	310.28	0.661	0.062
24912	57340	W1E1	441.05	-2094.75	-429.34	310.28	0.659	0.050
24912	57340	W1E1	444.72	-2112.16	-432.91	310.28	0.630	0.056
24912	57340	W1E1	448.51	-2130.18	-436.60	310.28	0.639	0.064
24912	57340	W1E1	452.31	-2148.19	-440.29	310.28	0.618	0.053
24912	57340	W1E1	456.03	-2165.87	-443.92	310.28	0.613	0.044
24912	57340	W1E1	459.68	-2183.19	-447.47	310.28	0.564	0.050
24912	57340	W1E1	463.32	-2200.47	-451.01	310.28	0.541	0.040
24912	57340	W1E1	467.08	-2218.36	-454.68	310.28	0.550	0.039
24912	57340	W1E1	470.84	-2236.20	-458.33	310.28	0.574	0.061
24912	57340	W1E1	474.73	-2254.67	-462.12	310.28	0.583	0.072
30614	56605	S1E1	375.13	313.24	1791.48	297.66	0.685	0.091
30614	56605	S1E1	378.85	316.35	1809.26	297.66	0.656	0.144
30614	56605	S1E1	382.65	319.52	1827.41	297.66	0.710	0.176
30614	56605	S1E1	386.27	322.54	1844.72	297.66	0.750	0.194
30614	56605	S1E1	389.97	325.63	1862.36	297.66	0.786	0.209
30614	56605	S1E1	393.52	328.60	1879.35	297.66	0.715	0.174
30614	56605	S1E1	397.09	331.58	1896.40	297.66	0.590	0.070
30614	56605	S1E1	400.73	334.62	1913.76	297.66	0.517	0.028
30614	56605	S1E1	404.43	337.71	1931.44	297.66	0.652	0.056
30614	56605	S1E1	408.20	340.86	1949.45	297.66	0.610	0.099
30614	56605	S1E1	412.10	344.11	1968.07	297.66	0.643	0.172
30614	56605	S1E1	415.79	347.19	1985.67	297.66	0.627	0.149
30614	56605	S1E1	419.54	350.32	2003.58	297.66	0.709	0.178
30614	56605	S1E1	423.12	353.31	2020.67	297.66	0.721	0.153
30614	56605	S1E1	426.63	356.25	2037.46	297.66	0.647	0.104
30614	56605	S1E1	430.27	359.28	2054.84	297.66	0.631	0.088
30614	56605	S1E1	433.91	362.32	2072.21	297.66	0.670	0.127
30614	56605	S1E1	437.48	365.30	2089.27	297.66	0.689	0.165
30614	56605	S1E1	440.98	368.23	2105.98	297.66	0.763	0.231
30614	56605	S1E1	444.47	371.14	2122.65	297.66	0.767	0.254
30614	56605	S1E1	448.08	374.16	2139.91	297.66	0.680	0.178
30614	56605	S1E1	451.69	377.17	2157.12	297.66	0.613	0.094
30614	56605	S1E1	455.42	380.28	2174.94	297.66	0.584	0.052
36861	56757	W1E2	211.86	896.33	501.55	168.11	0.895	0.120
36861	56757	W1E2	213.96	905.23	506.53	168.11	0.809	0.094

Table 5 continued

Table 5 (*continued*)

HD	Telescope		$10^{-6}B/\lambda$	u	v	Baseline		
Number	MJD	Pair	(rad $^{-1}$)	(arcsec $^{-1}$)	(arcsec $^{-1}$)	(m)	V^2	ΔV^2
(1)	(2)	(3)	(4)	(5)	(6)	(7)	(8)	(9)
36861	56757	W1E2	216.11	914.30	511.61	168.11	0.857	0.100
36861	56757	W1E2	218.15	922.96	516.46	168.11	0.766	0.093
36861	56757	W1E2	220.24	931.79	521.40	168.11	0.729	0.083
36861	56757	W1E2	222.25	940.29	526.16	168.11	0.818	0.090
36861	56757	W1E2	224.26	948.82	530.93	168.11	0.862	0.095
36861	56757	W1E2	226.32	957.51	535.79	168.11	0.784	0.080
36861	56757	W1E2	228.41	966.35	540.74	168.11	0.858	0.077
36861	56757	W1E2	230.54	975.37	545.78	168.11	0.878	0.075
36861	56757	W1E2	232.74	984.68	551.00	168.11	0.893	0.080
36861	56757	W1E2	234.82	993.49	555.92	168.11	0.910	0.096
36861	56757	W1E2	240.95	1019.40	570.42	168.11	0.950	0.109
36861	56757	W1E2	243.00	1028.10	575.29	168.11	0.943	0.097
36861	56757	W1E2	247.07	1045.32	584.93	168.11	0.995	0.094
36861	56757	W1E2	249.05	1053.68	589.61	168.11	0.959	0.089
36861	56757	W1E2	251.02	1062.02	594.27	168.11	0.844	0.082
36861	56757	W1E2	253.06	1070.66	599.10	168.11	0.851	0.090
36861	56757	W1E2	255.10	1079.27	603.92	168.11	0.724	0.088
36861	56757	W1E2	257.20	1088.18	608.91	168.11	0.585	0.067
36861	56757	W1E2	200.02	824.68	510.16	158.72	0.872	0.116
36861	56757	W1E2	202.00	832.86	515.23	158.72	0.877	0.099
36861	56757	W1E2	204.03	841.21	520.39	158.72	0.927	0.105
36861	56757	W1E2	205.96	849.18	525.32	158.72	0.798	0.096
36861	56757	W1E2	207.93	857.30	530.35	158.72	0.765	0.085
36861	56757	W1E2	209.83	865.12	535.18	158.72	0.877	0.094
36861	56757	W1E2	211.73	872.97	540.04	158.72	0.888	0.096
36861	56757	W1E2	213.67	880.96	544.98	158.72	0.832	0.084
36861	56757	W1E2	215.65	889.10	550.02	158.72	0.895	0.076
36861	56757	W1E2	217.66	897.39	555.15	158.72	0.901	0.072
36861	56757	W1E2	219.74	905.97	560.45	158.72	0.907	0.077
36861	56757	W1E2	221.70	914.07	565.46	158.72	0.961	0.097
36861	56757	W1E2	236.99	977.12	604.47	158.72	0.922	0.084
36861	56757	W1E2	238.92	985.07	609.38	158.72	0.936	0.095
36861	56757	W1E2	240.84	992.99	614.28	158.72	0.815	0.095
36861	56757	W1E2	242.83	1001.19	619.36	158.72	0.709	0.075
36861	56757	W1E2	380.87	740.68	1691.45	302.22	0.598	0.202
36861	56757	W1E2	384.65	748.04	1708.24	302.22	0.652	0.215
36861	56757	W1E2	388.51	755.54	1725.37	302.22	0.795	0.235
36861	56757	W1E2	392.19	762.69	1741.71	302.22	0.626	0.158
36861	56757	W1E2	395.94	769.99	1758.37	302.22	0.545	0.105
36861	56757	W1E2	399.55	777.01	1774.41	302.22	0.602	0.166
36861	56757	W1E2	403.18	784.06	1790.51	302.22	0.622	0.271
36861	56757	W1E2	406.87	791.24	1806.90	302.22	0.617	0.313
36861	56757	W1E2	410.63	798.55	1823.59	302.22	0.606	0.166
36861	56757	W1E2	414.46	806.00	1840.60	302.22	0.584	0.106
36861	56757	W1E2	418.41	813.70	1858.18	302.22	0.599	0.107

Table 5 continued

Table 5 (*continued*)

HD	Telescope		$10^{-6}B/\lambda$	u	v	Baseline	V^2	ΔV^2
Number	MJD	Pair	(rad $^{-1}$)	(arcsec $^{-1}$)	(arcsec $^{-1}$)	(m)	(8)	(9)
(1)	(2)	(3)	(4)	(5)	(6)	(7)		
36861	56757	W1E2	422.16	820.97	1874.79	302.22	0.616	0.118
36861	56757	W1E2	425.96	828.37	1891.70	302.22	0.554	0.071
36861	56757	W1E2	429.60	835.44	1907.84	302.22	0.534	0.060
36861	56757	W1E2	433.17	842.39	1923.70	302.22	0.546	0.059
36861	56757	W1E2	436.86	849.57	1940.10	302.22	0.513	0.049
36861	56757	W1E2	440.56	856.75	1956.51	302.22	0.496	0.048
36861	56757	W1E2	444.18	863.80	1972.61	302.22	0.509	0.052
36861	56757	W1E2	447.73	870.71	1988.39	302.22	0.477	0.051
36861	56757	W1E2	451.28	877.60	2004.13	302.22	0.508	0.059
36861	56757	W1E2	454.95	884.74	2020.42	302.22	0.539	0.071
36861	56757	W1E2	458.61	891.85	2036.67	302.22	0.511	0.063
36861	56757	W1E2	462.39	899.22	2053.49	302.22	0.486	0.060
36861	56602	E1S1	374.97	1779.71	370.70	297.54	0.392	0.114
36861	56602	E1S1	378.69	1797.38	374.38	297.54	0.404	0.107
36861	56602	E1S1	382.49	1815.40	378.13	297.54	0.464	0.141
36861	56602	E1S1	386.11	1832.60	381.71	297.54	0.505	0.151
36861	56602	E1S1	389.81	1850.13	385.36	297.54	0.519	0.148
36861	56602	E1S1	393.36	1867.01	388.88	297.54	0.453	0.093
36861	56602	E1S1	396.93	1883.94	392.41	297.54	0.558	0.139
36861	56602	E1S1	400.56	1901.19	396.00	297.54	0.566	0.131
36861	56602	E1S1	404.27	1918.75	399.66	297.54	0.549	0.121
36861	56602	E1S1	408.04	1936.65	403.38	297.54	0.603	0.125
36861	56602	E1S1	411.93	1955.15	407.24	297.54	0.567	0.085
36861	56602	E1S1	415.62	1972.63	410.88	297.54	0.636	0.092
36861	56602	E1S1	419.36	1990.42	414.58	297.54	0.688	0.140
36861	56602	E1S1	422.94	2007.40	418.12	297.54	0.845	0.217
36861	56602	E1S1	426.46	2024.08	421.60	297.54	0.853	0.213
36861	56602	E1S1	430.09	2041.35	425.19	297.54	0.814	0.173
36861	56602	E1S1	433.73	2058.60	428.79	297.54	0.836	0.161
36861	56602	E1S1	437.30	2075.55	432.32	297.54	0.715	0.110
36861	56602	E1S1	440.80	2092.15	435.77	297.54	0.705	0.096
36861	56602	E1S1	444.29	2108.71	439.22	297.54	0.645	0.091
36861	56602	E1S1	447.90	2125.85	442.79	297.54	0.631	0.093
36861	56602	E1S1	451.50	2142.95	446.35	297.54	0.685	0.116
36861	56602	E1S1	455.23	2160.65	450.04	297.54	0.661	0.112
36861	56603	W1E1	391.00	1846.64	428.21	310.26	0.492	0.144
36861	56603	W1E1	394.89	1864.98	432.46	310.26	0.532	0.141
36861	56603	W1E1	398.85	1883.68	436.79	310.26	0.593	0.182
36861	56603	W1E1	402.62	1901.52	440.93	310.26	0.673	0.202
36861	56603	W1E1	406.47	1919.71	445.15	310.26	0.732	0.209
36861	56603	W1E1	410.18	1937.22	449.21	310.26	0.628	0.128
36861	56603	W1E1	413.90	1954.79	453.28	310.26	0.714	0.179
36861	56603	W1E1	417.69	1972.69	457.43	310.26	0.626	0.148
36861	56603	W1E1	421.55	1990.91	461.66	310.26	0.572	0.130
36861	56603	W1E1	425.48	2009.48	465.97	310.26	0.685	0.146

Table 5 continued

Table 5 (*continued*)

HD	Telescope		$10^{-6}B/\lambda$	u	v	Baseline		
Number	MJD	Pair	(rad $^{-1}$)	(arcsec $^{-1}$)	(arcsec $^{-1}$)	(m)	V^2	ΔV^2
(1)	(2)	(3)	(4)	(5)	(6)	(7)	(8)	(9)
36861	56603	W1E1	429.55	2028.67	470.42	310.26	0.656	0.103
36861	56603	W1E1	433.39	2046.81	474.62	310.26	0.737	0.111
36861	56603	W1E1	437.30	2065.27	478.90	310.26	0.704	0.147
36861	56603	W1E1	441.03	2082.89	482.99	310.26	0.726	0.191
36861	56603	W1E1	444.69	2100.20	487.00	310.26	0.681	0.176
36861	56603	W1E1	448.48	2118.11	491.16	310.26	0.699	0.153
36861	56603	W1E1	452.28	2136.02	495.31	310.26	0.777	0.154
36861	56603	W1E1	456.00	2153.60	499.39	310.26	0.706	0.113
36861	56603	W1E1	459.65	2170.83	503.38	310.26	0.729	0.103
36861	56603	W1E1	463.28	2188.01	507.36	310.26	0.727	0.105
36861	56603	W1E1	467.05	2205.80	511.49	310.26	0.712	0.107
36861	56603	W1E1	470.81	2223.54	515.60	310.26	0.679	0.118
36861	56603	W1E1	474.70	2241.91	519.86	310.26	0.530	0.093
36861	56603	W1E1	394.07	1856.24	452.17	312.70	0.469	0.136
36861	56603	W1E1	397.98	1874.67	456.65	312.70	0.486	0.128
36861	56603	W1E1	401.97	1893.46	461.23	312.70	0.555	0.171
36861	56603	W1E1	405.78	1911.40	465.60	312.70	0.642	0.194
36861	56603	W1E1	409.66	1929.68	470.06	312.70	0.687	0.197
36861	56603	W1E1	413.40	1947.28	474.34	312.70	0.587	0.121
36861	56603	W1E1	417.15	1964.95	478.65	312.70	0.658	0.166
36861	56603	W1E1	420.97	1982.94	483.03	312.70	0.542	0.131
36861	56603	W1E1	424.86	2001.26	487.49	312.70	0.497	0.117
36861	56603	W1E1	428.82	2019.92	492.04	312.70	0.621	0.135
36861	56603	W1E1	432.92	2039.21	496.74	312.70	0.577	0.093
36861	56603	W1E1	436.79	2057.44	501.18	312.70	0.643	0.099
36861	56603	W1E1	440.73	2076.00	505.70	312.70	0.605	0.127
36861	56603	W1E1	444.49	2093.71	510.01	312.70	0.575	0.154
36861	56603	W1E1	448.18	2111.11	514.25	312.70	0.566	0.149
36861	56603	W1E1	452.00	2129.12	518.64	312.70	0.624	0.140
36861	56603	W1E1	455.83	2147.12	523.02	312.70	0.674	0.137
36861	56603	W1E1	459.58	2164.79	527.33	312.70	0.617	0.102
36861	56603	W1E1	463.25	2182.11	531.55	312.70	0.639	0.093
36861	56603	W1E1	466.92	2199.38	535.75	312.70	0.646	0.095
36861	56603	W1E1	470.72	2217.26	540.11	312.70	0.620	0.095
36861	56603	W1E1	474.50	2235.09	544.45	312.70	0.581	0.102
36861	56603	W1E1	478.42	2253.56	548.95	312.70	0.424	0.077
36861	56756	W1E2	216.72	925.29	497.76	171.97	0.985	0.273
36861	56756	W1E2	218.87	934.47	502.70	171.97	0.841	0.143
36861	56756	W1E2	221.06	943.84	507.74	171.97	0.846	0.146
36861	56756	W1E2	223.16	952.78	512.55	171.97	0.841	0.181
36861	56756	W1E2	225.29	961.90	517.46	171.97	0.797	0.167
36861	56756	W1E2	227.35	970.67	522.18	171.97	0.755	0.124
36861	56756	W1E2	229.41	979.48	526.91	171.97	0.779	0.104
36861	56756	W1E2	231.51	988.44	531.74	171.97	0.911	0.140
36861	56756	W1E2	233.65	997.57	536.65	171.97	0.933	0.135

Table 5 continued

Table 5 (*continued*)

HD	Telescope		$10^{-6}B/\lambda$	u	v	Baseline	V^2	ΔV^2
Number	MJD	Pair	(rad $^{-1}$)	(arcsec $^{-1}$)	(arcsec $^{-1}$)	(m)	(8)	(9)
(1)	(2)	(3)	(4)	(5)	(6)	(7)		
36861	56756	W1E2	235.83	1006.88	541.65	171.97	0.883	0.095
36861	56756	W1E2	238.08	1016.50	546.83	171.97	0.848	0.080
36861	56756	W1E2	240.21	1025.58	551.72	171.97	0.902	0.086
36861	56756	W1E2	242.38	1034.83	556.69	171.97	0.934	0.108
36861	56756	W1E2	250.68	1070.28	575.76	171.97	0.981	0.103
36861	56756	W1E2	252.74	1079.09	580.50	171.97	0.885	0.080
36861	56756	W1E2	254.76	1087.73	585.15	171.97	0.790	0.066
36861	56756	W1E2	256.78	1096.33	589.78	171.97	0.779	0.061
36861	56756	W1E2	258.87	1105.25	594.57	171.97	0.754	0.062
36861	56756	W1E2	260.95	1114.13	599.35	171.97	0.869	0.097
36861	56756	W1E2	263.11	1123.34	604.31	171.97	0.880	0.118
36861	56756	W1E2	203.55	846.24	507.68	161.52	1.000	0.277
36861	56756	W1E2	205.57	854.64	512.72	161.52	0.835	0.142
36861	56756	W1E2	207.63	863.21	517.86	161.52	0.782	0.135
36861	56756	W1E2	209.60	871.39	522.77	161.52	0.816	0.174
36861	56756	W1E2	211.61	879.72	527.77	161.52	0.824	0.172
36861	56756	W1E2	213.54	887.75	532.58	161.52	0.805	0.131
36861	56756	W1E2	215.47	895.80	537.41	161.52	0.759	0.102
36861	56756	W1E2	217.45	904.00	542.33	161.52	0.840	0.131
36861	56756	W1E2	219.45	912.35	547.35	161.52	0.882	0.129
36861	56756	W1E2	221.50	920.86	552.45	161.52	0.886	0.097
36861	56756	W1E2	223.62	929.66	557.73	161.52	0.895	0.085
36861	56756	W1E2	225.62	937.97	562.71	161.52	0.904	0.088
36861	56756	W1E2	227.65	946.43	567.79	161.52	0.919	0.108
36861	56756	W1E2	235.45	978.85	587.24	161.52	0.969	0.103
36861	56756	W1E2	237.39	986.91	592.07	161.52	0.890	0.082
36861	56756	W1E2	239.29	994.80	596.81	161.52	0.883	0.074
36861	56756	W1E2	241.18	1002.68	601.53	161.52	0.865	0.069
36861	56756	W1E2	243.14	1010.83	606.42	161.52	0.808	0.067
36861	56756	W1E2	245.10	1018.96	611.30	161.52	0.894	0.100
36861	56756	W1E2	247.12	1027.38	616.35	161.52	0.842	0.114
37742	57340	W1E1	348.55	-1631.83	-438.96	276.58	0.056	0.022
37742	57340	W1E1	352.01	-1648.03	-443.32	276.58	0.054	0.020
37742	57340	W1E1	355.54	-1664.55	-447.77	276.58	0.057	0.021
37742	57340	W1E1	358.91	-1680.32	-452.01	276.58	0.049	0.016
37742	57340	W1E1	362.34	-1696.39	-456.33	276.58	0.045	0.015
37742	57340	W1E1	365.65	-1711.87	-460.49	276.58	0.045	0.015
37742	57340	W1E1	368.97	-1727.40	-464.67	276.58	0.052	0.019
37742	57340	W1E1	372.34	-1743.21	-468.92	276.58	0.062	0.024
37742	57340	W1E1	375.78	-1759.31	-473.26	276.58	0.056	0.021
37742	57340	W1E1	379.29	-1775.72	-477.67	276.58	0.044	0.013
37742	57340	W1E1	382.91	-1792.68	-482.23	276.58	0.032	0.008
37742	57340	W1E1	386.34	-1808.71	-486.54	276.58	0.030	0.008
37742	57340	W1E1	389.82	-1825.03	-490.93	276.58	0.036	0.010
37742	57340	W1E1	393.15	-1840.59	-495.12	276.58	0.037	0.009

Table 5 continued

Table 5 (*continued*)

HD	Telescope		$10^{-6}B/\lambda$	u	v	Baseline	V^2	ΔV^2
Number	MJD	Pair	(rad $^{-1}$)	(arcsec $^{-1}$)	(arcsec $^{-1}$)	(m)	(8)	(9)
(1)	(2)	(3)	(4)	(5)	(6)	(7)		
37742	57340	W1E1	396.41	-1855.89	-499.24	276.58	0.035	0.007
37742	57340	W1E1	399.79	-1871.72	-503.49	276.58	0.033	0.007
37742	57340	W1E1	403.17	-1887.54	-507.75	276.58	0.029	0.006
37742	57340	W1E1	406.49	-1903.08	-511.93	276.58	0.026	0.005
37742	57340	W1E1	409.74	-1918.30	-516.03	276.58	0.024	0.005
37742	57340	W1E1	412.99	-1933.49	-520.11	276.58	0.026	0.006
37742	57340	W1E1	416.34	-1949.20	-524.34	276.58	0.023	0.006
37742	57340	W1E1	419.69	-1964.88	-528.55	276.58	0.016	0.004
37742	57340	W1E1	423.16	-1981.11	-532.92	276.58	0.018	0.005
149757	57933	S2E2	295.58	1187.43	-802.22	234.54	0.165	0.091
149757	57933	S2E2	298.52	1199.21	-810.18	234.54	0.129	0.071
149757	57933	S2E2	301.51	1211.24	-818.31	234.54	0.114	0.082
149757	57933	S2E2	304.36	1222.71	-826.06	234.54	0.107	0.057
149757	57933	S2E2	307.28	1234.41	-833.96	234.54	0.115	0.037
149757	57933	S2E2	310.08	1245.67	-841.57	234.54	0.148	0.027
149757	57933	S2E2	312.89	1256.97	-849.20	234.54	0.162	0.048
149757	57933	S2E2	315.76	1268.47	-856.98	234.54	0.153	0.055
149757	57933	S2E2	318.67	1280.19	-864.89	234.54	0.110	0.064
149757	57933	S2E2	321.65	1292.13	-872.96	234.54	0.108	0.063
149757	57933	S2E2	324.72	1304.48	-881.30	234.54	0.105	0.046
149757	57933	S2E2	327.62	1316.14	-889.18	234.54	0.123	0.051
149757	57933	S2E2	330.58	1328.01	-897.20	234.54	0.129	0.068
149757	57933	S2E2	333.40	1339.34	-904.85	234.54	0.122	0.036
149757	57933	S2E2	336.17	1350.47	-912.37	234.54	0.130	0.042
149757	57933	S2E2	339.03	1361.99	-920.15	234.54	0.132	0.060
149757	57933	S2E2	341.90	1373.50	-927.93	234.54	0.130	0.054
149757	57933	S2E2	344.71	1384.81	-935.57	234.54	0.141	0.043
149757	57933	S2E2	347.47	1395.89	-943.05	234.54	0.148	0.050
149757	57933	S2E2	350.22	1406.93	-950.52	234.54	0.150	0.035
149757	57933	S2E2	353.07	1418.37	-958.24	234.54	0.152	0.027
149757	57933	S2E2	355.91	1429.78	-965.95	234.54	0.135	0.042
149757	57933	S2E2	358.85	1441.59	-973.93	234.54	0.115	0.056
149757	57933	S2E2	306.60	1228.85	-836.35	243.29	0.218	0.047
149757	57933	S2E2	309.65	1241.05	-844.65	243.29	0.198	0.031
149757	57933	S2E2	312.75	1253.50	-853.12	243.29	0.226	0.036
149757	57933	S2E2	315.72	1265.37	-861.20	243.29	0.239	0.039
149757	57933	S2E2	318.73	1277.47	-869.44	243.29	0.195	0.029
149757	57933	S2E2	321.64	1289.13	-877.37	243.29	0.171	0.023
149757	57933	S2E2	324.56	1300.82	-885.33	243.29	0.172	0.029
149757	57933	S2E2	327.53	1312.73	-893.43	243.29	0.180	0.018
149757	57933	S2E2	330.56	1324.86	-901.69	243.29	0.186	0.025
149757	57933	S2E2	333.64	1337.21	-910.10	243.29	0.202	0.030
149757	57933	S2E2	336.83	1349.99	-918.79	243.29	0.188	0.022
149757	57933	S2E2	339.84	1362.06	-927.00	243.29	0.182	0.018
149757	57933	S2E2	342.90	1374.34	-935.37	243.29	0.179	0.027

Table 5 continued

Table 5 (*continued*)

HD	Telescope		$10^{-6}B/\lambda$	u	v	Baseline	V^2	ΔV^2
Number	MJD	Pair	(rad $^{-1}$)	(arcsec $^{-1}$)	(arcsec $^{-1}$)	(m)	(8)	(9)
(1)	(2)	(3)	(4)	(5)	(6)	(7)		
149757	57933	S2E2	345.83	1386.06	-943.34	243.29	0.184	0.024
149757	57933	S2E2	348.70	1397.59	-951.19	243.29	0.177	0.029
149757	57933	S2E2	351.68	1409.51	-959.30	243.29	0.137	0.032
149757	57933	S2E2	354.65	1421.42	-967.41	243.29	0.128	0.042
149757	57933	S2E2	357.57	1433.12	-975.37	243.29	0.125	0.046
149757	57933	S2E2	360.43	1444.59	-983.17	243.29	0.124	0.046
149757	57933	S2E2	363.28	1456.02	-990.95	243.29	0.121	0.052
149757	57933	S2E2	366.24	1467.85	-999.01	243.29	0.114	0.027
149757	57933	S2E2	369.18	1479.66	-1007.04	243.29	0.124	0.041
149757	57933	S2E2	372.23	1491.88	-1015.36	243.29	0.120	0.030
149757	57933	S2E2	310.66	1239.40	-855.75	246.51	0.218	0.088
149757	57933	S2E2	313.75	1251.70	-864.25	246.51	0.209	0.080
149757	57933	S2E2	316.89	1264.26	-872.91	246.51	0.211	0.036
149757	57933	S2E2	319.89	1276.23	-881.18	246.51	0.226	0.058
149757	57933	S2E2	322.95	1288.44	-889.61	246.51	0.188	0.046
149757	57933	S2E2	325.90	1300.19	-897.73	246.51	0.155	0.028
149757	57933	S2E2	328.86	1311.99	-905.87	246.51	0.136	0.023
149757	57933	S2E2	331.87	1324.00	-914.16	246.51	0.143	0.017
149757	57933	S2E2	334.93	1336.23	-922.61	246.51	0.165	0.024
149757	57933	S2E2	338.06	1348.69	-931.21	246.51	0.174	0.053
149757	57933	S2E2	341.28	1361.57	-940.11	246.51	0.161	0.055
149757	57933	S2E2	344.34	1373.75	-948.51	246.51	0.149	0.023
149757	57933	S2E2	347.44	1386.14	-957.07	246.51	0.144	0.015
149757	57933	S2E2	350.40	1397.96	-965.23	246.51	0.143	0.020
149757	57933	S2E2	353.32	1409.58	-973.25	246.51	0.128	0.022
149757	57933	S2E2	356.33	1421.60	-981.55	246.51	0.116	0.018
149757	57933	S2E2	359.34	1433.62	-989.85	246.51	0.105	0.012
149757	57933	S2E2	362.30	1445.42	-998.00	246.51	0.091	0.026
149757	57933	S2E2	365.20	1456.98	-1005.98	246.51	0.081	0.029
149757	57933	S2E2	368.09	1468.51	-1013.95	246.51	0.079	0.032
149757	57933	S2E2	371.08	1480.45	-1022.19	246.51	0.066	0.030
149757	57933	S2E2	374.07	1492.36	-1030.41	246.51	0.082	0.026
149757	57933	S2E2	377.16	1504.69	-1038.92	246.51	0.084	0.015
149757	57933	S2E2	246.69	-612.39	-1027.28	195.75	0.411	0.090
149757	57933	S2E2	249.13	-618.47	-1037.48	195.75	0.377	0.185
149757	57933	S2E2	251.63	-624.67	-1047.89	195.75	0.368	0.170
149757	57933	S2E2	254.02	-630.59	-1057.81	195.75	0.320	0.115
149757	57933	S2E2	256.45	-636.62	-1067.93	195.75	0.273	0.078
149757	57933	S2E2	258.79	-642.43	-1077.67	195.75	0.271	0.082
149757	57933	S2E2	261.13	-648.25	-1087.45	195.75	0.297	0.084
149757	57933	S2E2	263.52	-654.19	-1097.40	195.75	0.311	0.078
149757	57933	S2E2	265.96	-660.23	-1107.54	195.75	0.314	0.054
149757	57933	S2E2	268.44	-666.39	-1117.87	195.75	0.292	0.048
149757	57933	S2E2	271.00	-672.76	-1128.55	195.75	0.241	0.031
149757	57933	S2E2	273.43	-678.77	-1138.64	195.75	0.233	0.032

Table 5 continued

Table 5 (*continued*)

HD	Telescope		$10^{-6}B/\lambda$	u	v	Baseline		
Number	MJD	Pair	(rad $^{-1}$)	(arcsec $^{-1}$)	(arcsec $^{-1}$)	(m)	V^2	ΔV^2
(1)	(2)	(3)	(4)	(5)	(6)	(7)	(8)	(9)
149757	57933	S2E2	275.89	-684.89	-1148.91	195.75	0.255	0.044
149757	57933	S2E2	278.24	-690.73	-1158.71	195.75	0.268	0.049
149757	57933	S2E2	280.56	-696.48	-1168.34	195.75	0.235	0.038
149757	57933	S2E2	282.95	-702.42	-1178.30	195.75	0.205	0.030
149757	57933	S2E2	285.34	-708.35	-1188.27	195.75	0.184	0.028
149757	57933	S2E2	287.69	-714.18	-1198.05	195.75	0.160	0.030
149757	57933	S2E2	289.99	-719.90	-1207.63	195.75	0.143	0.040
149757	57933	S2E2	292.29	-725.60	-1217.19	195.75	0.109	0.040
149757	57933	S2E2	294.66	-731.49	-1227.08	195.75	0.153	0.052
149757	57933	S2E2	297.03	-737.38	-1236.95	195.75	0.170	0.034
149757	57933	S2E2	299.49	-743.47	-1247.17	195.75	0.168	0.026
149757	57573	S2W1	235.14	-519.63	-1014.65	186.58	0.310	0.082
149757	57573	S2W1	237.47	-524.79	-1024.72	186.58	0.326	0.094
149757	57573	S2W1	239.85	-530.06	-1035.00	186.58	0.317	0.098
149757	57573	S2W1	242.12	-535.08	-1044.80	186.58	0.318	0.062
149757	57573	S2W1	244.44	-540.19	-1054.79	186.58	0.276	0.068
149757	57573	S2W1	246.67	-545.12	-1064.41	186.58	0.245	0.063
149757	57573	S2W1	248.91	-550.07	-1074.07	186.58	0.260	0.054
149757	57573	S2W1	251.18	-555.10	-1083.90	186.58	0.264	0.051
149757	57573	S2W1	253.51	-560.23	-1093.92	186.58	0.276	0.037
149757	57573	S2W1	255.87	-565.46	-1104.12	186.58	0.254	0.039
149757	57573	S2W1	258.31	-570.86	-1114.67	186.58	0.230	0.027
149757	57573	S2W1	260.62	-575.96	-1124.63	186.58	0.220	0.028
149757	57573	S2W1	262.97	-581.16	-1134.78	186.58	0.223	0.048
149757	57573	S2W1	265.22	-586.11	-1144.45	186.58	0.233	0.043
149757	57573	S2W1	267.42	-590.98	-1153.97	186.58	0.211	0.037
149757	57573	S2W1	269.70	-596.02	-1163.81	186.58	0.181	0.027
149757	57573	S2W1	271.98	-601.06	-1173.65	186.58	0.147	0.025
149757	57573	S2W1	274.22	-606.01	-1183.31	186.58	0.134	0.027
149757	57573	S2W1	276.41	-610.86	-1192.77	186.58	0.108	0.035
149757	57573	S2W1	278.60	-615.69	-1202.21	186.58	0.107	0.062
149757	57573	S2W1	280.87	-620.70	-1211.99	186.58	0.129	0.040
149757	57573	S2W1	283.13	-625.69	-1221.73	186.58	0.155	0.029
149757	57573	S2W1	285.47	-630.86	-1231.83	186.58	0.145	0.023
149757	57573	S2W1	226.83	-443.23	-1006.41	179.99	0.349	0.059
149757	57573	S2W1	229.08	-447.63	-1016.40	179.99	0.399	0.067
149757	57573	S2W1	231.38	-452.12	-1026.59	179.99	0.406	0.081
149757	57573	S2W1	233.57	-456.40	-1036.32	179.99	0.431	0.093
149757	57573	S2W1	235.80	-460.77	-1046.23	179.99	0.351	0.088
149757	57573	S2W1	237.95	-464.97	-1055.77	179.99	0.273	0.071
149757	57573	S2W1	240.11	-469.19	-1065.35	179.99	0.290	0.048
149757	57573	S2W1	242.31	-473.48	-1075.10	179.99	0.340	0.085
149757	57573	S2W1	244.55	-477.86	-1085.03	179.99	0.359	0.052
149757	57573	S2W1	246.83	-482.31	-1095.15	179.99	0.315	0.039
149757	57573	S2W1	249.19	-486.92	-1105.61	179.99	0.282	0.034

Table 5 continued

Table 5 (*continued*)

HD	Telescope		$10^{-6}B/\lambda$	u	v	Baseline	V^2	ΔV^2
Number	MJD	Pair	(rad $^{-1}$)	(arcsec $^{-1}$)	(arcsec $^{-1}$)	(m)	(8)	(9)
(1)	(2)	(3)	(4)	(5)	(6)	(7)		
149757	57573	S2W1	251.41	-491.28	-1115.50	179.99	0.250	0.042
149757	57573	S2W1	253.68	-495.71	-1125.56	179.99	0.271	0.069
149757	57573	S2W1	255.85	-499.93	-1135.16	179.99	0.285	0.045
149757	57573	S2W1	257.97	-504.09	-1144.60	179.99	0.258	0.038
149757	57573	S2W1	260.17	-508.39	-1154.36	179.99	0.226	0.033
149757	57573	S2W1	262.37	-512.69	-1164.12	179.99	0.186	0.041
149757	57573	S2W1	264.53	-516.91	-1173.70	179.99	0.161	0.030
149757	57573	S2W1	266.65	-521.04	-1183.09	179.99	0.151	0.042
149757	57573	S2W1	268.76	-525.17	-1192.45	179.99	0.144	0.087
149757	57573	S2W1	270.94	-529.44	-1202.15	179.99	0.156	0.058
149757	57573	S2W1	273.12	-533.69	-1211.81	179.99	0.173	0.073
149757	57573	S2W1	275.38	-538.10	-1221.83	179.99	0.183	0.032
149757	57573	S2W1	216.74	-331.19	-997.22	171.98	0.376	0.064
149757	57573	S2W1	218.89	-334.48	-1007.12	171.98	0.381	0.075
149757	57573	S2W1	221.09	-337.83	-1017.22	171.98	0.413	0.091
149757	57573	S2W1	223.18	-341.03	-1026.86	171.98	0.421	0.137
149757	57573	S2W1	225.31	-344.29	-1036.68	171.98	0.326	0.085
149757	57573	S2W1	227.37	-347.43	-1046.14	171.98	0.288	0.091
149757	57573	S2W1	229.43	-350.58	-1055.63	171.98	0.333	0.089
149757	57573	S2W1	231.53	-353.79	-1065.29	171.98	0.371	0.063
149757	57573	S2W1	233.67	-357.06	-1075.13	171.98	0.355	0.080
149757	57573	S2W1	235.85	-360.39	-1085.16	171.98	0.325	0.042
149757	57573	S2W1	238.10	-363.83	-1095.53	171.98	0.327	0.067
149757	57573	S2W1	240.23	-367.09	-1105.32	171.98	0.296	0.046
149757	57573	S2W1	242.40	-370.40	-1115.29	171.98	0.323	0.072
149757	57573	S2W1	244.47	-373.56	-1124.80	171.98	0.303	0.071
149757	57573	S2W1	246.50	-376.66	-1134.15	171.98	0.278	0.045
149757	57573	S2W1	248.60	-379.87	-1143.82	171.98	0.239	0.050
149757	57573	S2W1	250.70	-383.09	-1153.50	171.98	0.196	0.038
149757	57573	S2W1	252.77	-386.24	-1162.99	171.98	0.172	0.054
149757	57573	S2W1	254.79	-389.33	-1172.29	171.98	0.163	0.060
149757	57573	S2W1	256.81	-392.41	-1181.57	171.98	0.108	0.061
149757	57573	S2W1	258.89	-395.60	-1191.18	171.98	0.182	0.122
149757	57573	S2W1	260.98	-398.78	-1200.76	171.98	0.184	0.091
149757	57573	S2W1	263.13	-402.08	-1210.68	171.98	0.209	0.050
149757	57573	S2W1	210.46	-239.23	-991.91	167.00	0.323	0.055
149757	57573	S2W1	212.55	-241.60	-1001.76	167.00	0.298	0.056
149757	57573	S2W1	214.68	-244.02	-1011.81	167.00	0.346	0.056
149757	57573	S2W1	216.72	-246.34	-1021.39	167.00	0.334	0.052
149757	57573	S2W1	218.79	-248.69	-1031.16	167.00	0.285	0.058
149757	57573	S2W1	220.79	-250.96	-1040.57	167.00	0.287	0.063
149757	57573	S2W1	222.79	-253.24	-1050.01	167.00	0.313	0.052
149757	57573	S2W1	224.83	-255.56	-1059.62	167.00	0.321	0.046
149757	57573	S2W1	226.91	-257.92	-1069.41	167.00	0.296	0.059
149757	57573	S2W1	229.02	-260.32	-1079.38	167.00	0.278	0.040

Table 5 continued

Table 5 (*continued*)

HD	Telescope		$10^{-6}B/\lambda$	u	v	Baseline		
Number	MJD	Pair	(rad $^{-1}$)	(arcsec $^{-1}$)	(arcsec $^{-1}$)	(m)	V^2	ΔV^2
(1)	(2)	(3)	(4)	(5)	(6)	(7)	(8)	(9)
149757	57573	S2W1	231.21	-262.81	-1089.69	167.00	0.266	0.054
149757	57573	S2W1	233.28	-265.16	-1099.43	167.00	0.237	0.036
149757	57573	S2W1	235.38	-267.55	-1109.35	167.00	0.222	0.037
149757	57573	S2W1	237.39	-269.83	-1118.81	167.00	0.205	0.034
149757	57573	S2W1	239.36	-272.08	-1128.11	167.00	0.237	0.037
149757	57573	S2W1	241.40	-274.40	-1137.73	167.00	0.213	0.039
149757	57573	S2W1	243.44	-276.72	-1147.35	167.00	0.190	0.042
149757	57573	S2W1	245.45	-278.99	-1156.80	167.00	0.189	0.040
149757	57573	S2W1	247.41	-281.23	-1166.05	167.00	0.201	0.066
149757	57573	S2W1	249.37	-283.45	-1175.28	167.00	0.179	0.057
149757	57573	S2W1	251.40	-285.75	-1184.83	167.00	0.250	0.069
149757	57573	S2W1	253.42	-288.05	-1194.36	167.00	0.200	0.037
149757	57573	S2W1	255.51	-290.43	-1204.23	167.00	0.189	0.031
149757	57573	S2W1	205.89	-140.66	-988.22	163.37	0.419	0.081
149757	57573	S2W1	207.93	-142.06	-998.03	163.37	0.362	0.062
149757	57573	S2W1	210.02	-143.48	-1008.04	163.37	0.364	0.062
149757	57573	S2W1	212.01	-144.84	-1017.59	163.37	0.370	0.058
149757	57573	S2W1	214.04	-146.23	-1027.32	163.37	0.385	0.075
149757	57573	S2W1	215.99	-147.56	-1036.69	163.37	0.441	0.091
149757	57573	S2W1	217.95	-148.90	-1046.10	163.37	0.439	0.080
149757	57573	S2W1	219.94	-150.26	-1055.68	163.37	0.384	0.055
149757	57573	S2W1	221.98	-151.65	-1065.43	163.37	0.358	0.054
149757	57573	S2W1	224.05	-153.07	-1075.36	163.37	0.373	0.047
149757	57573	S2W1	226.19	-154.53	-1085.64	163.37	0.359	0.044
149757	57573	S2W1	228.21	-155.91	-1095.34	163.37	0.369	0.069
149757	57573	S2W1	230.27	-157.32	-1105.22	163.37	0.356	0.058
149757	57573	S2W1	232.23	-158.66	-1114.65	163.37	0.351	0.078
149757	57573	S2W1	234.16	-159.98	-1123.92	163.37	0.369	0.051
149757	57573	S2W1	236.16	-161.34	-1133.50	163.37	0.343	0.047
149757	57573	S2W1	238.15	-162.70	-1143.08	163.37	0.343	0.106
149757	57573	S2W1	240.11	-164.04	-1152.49	163.37	0.341	0.090
149757	57573	S2W1	242.04	-165.36	-1161.71	163.37	0.307	0.164
149757	57573	S2W1	243.95	-166.66	-1170.91	163.37	0.287	0.080
149757	57573	S2W1	245.93	-168.02	-1180.42	163.37	0.344	0.085
149757	57573	S2W1	247.91	-169.37	-1189.92	163.37	0.302	0.044
149757	57573	S2W1	249.96	-170.77	-1199.75	163.37	0.307	0.042
149757	57573	S2W1	203.46	-11.78	-986.32	161.44	0.493	0.108
149757	57573	S2W1	205.48	-11.89	-996.11	161.44	0.468	0.100
149757	57573	S2W1	207.54	-12.01	-1006.10	161.44	0.490	0.100
149757	57573	S2W1	209.50	-12.13	-1015.63	161.44	0.453	0.090
149757	57573	S2W1	211.51	-12.24	-1025.34	161.44	0.405	0.101
149757	57573	S2W1	213.44	-12.36	-1034.70	161.44	0.455	0.152
149757	57573	S2W1	215.37	-12.47	-1044.08	161.44	0.462	0.099
149757	57573	S2W1	217.34	-12.58	-1053.64	161.44	0.446	0.078
149757	57573	S2W1	219.35	-12.70	-1063.38	161.44	0.419	0.072

Table 5 continued

Table 5 (*continued*)

HD	Telescope		$10^{-6}B/\lambda$	u	v	Baseline	V^2	ΔV^2
Number	MJD	Pair	(rad $^{-1}$)	(arcsec $^{-1}$)	(arcsec $^{-1}$)	(m)	(8)	(9)
(1)	(2)	(3)	(4)	(5)	(6)	(7)		
149757	57573	S2W1	221.40	-12.82	-1073.29	161.44	0.412	0.061
149757	57573	S2W1	223.51	-12.94	-1083.54	161.44	0.378	0.053
149757	57573	S2W1	225.51	-13.05	-1093.23	161.44	0.374	0.056
149757	57573	S2W1	227.55	-13.17	-1103.09	161.44	0.379	0.063
149757	57573	S2W1	229.49	-13.28	-1112.50	161.44	0.430	0.084
149757	57573	S2W1	231.39	-13.39	-1121.75	161.44	0.377	0.064
149757	57573	S2W1	233.37	-13.51	-1131.32	161.44	0.319	0.050
149757	57573	S2W1	235.34	-13.62	-1140.88	161.44	0.271	0.048
149757	57573	S2W1	237.28	-13.74	-1150.27	161.44	0.245	0.053
149757	57573	S2W1	239.18	-13.85	-1159.47	161.44	0.177	0.051
149757	57573	S2W1	241.07	-13.95	-1168.65	161.44	0.210	0.082
149757	57573	S2W1	243.03	-14.07	-1178.15	161.44	0.294	0.088
149757	57573	S2W1	244.98	-14.18	-1187.62	161.44	0.308	0.056
149757	57573	S2W1	247.01	-14.30	-1197.44	161.44	0.311	0.056
214680	56637	S1E1	395.84	-1255.82	-1451.16	314.10	0.934	0.071
214680	56637	S1E1	399.77	-1268.29	-1465.56	314.10	0.966	0.100
214680	56637	S1E1	403.78	-1281.00	-1480.26	314.10	0.923	0.078
214680	56637	S1E1	407.61	-1293.14	-1494.28	314.10	0.900	0.084
214680	56637	S1E1	411.50	-1305.51	-1508.57	314.10	0.923	0.106
214680	56637	S1E1	415.26	-1317.42	-1522.33	314.10	0.881	0.072
214680	56637	S1E1	419.02	-1329.37	-1536.14	314.10	0.945	0.072
214680	56637	S1E1	422.86	-1341.54	-1550.21	314.10	0.975	0.066
214680	56637	S1E1	426.77	-1353.93	-1564.53	314.10	0.969	0.063
214680	56637	S1E1	430.75	-1366.56	-1579.12	314.10	0.939	0.055
214680	56637	S1E1	434.86	-1379.61	-1594.20	314.10	0.930	0.057
214680	56637	S1E1	438.75	-1391.94	-1608.46	314.10	0.865	0.059
214680	56637	S1E1	442.71	-1404.50	-1622.96	314.10	0.871	0.080
214680	56637	S1E1	446.48	-1416.48	-1636.81	314.10	0.910	0.088
214680	56637	S1E1	450.19	-1428.25	-1650.41	314.10	0.951	0.057
214680	56637	S1E1	454.03	-1440.44	-1664.49	314.10	0.945	0.062
214680	56637	S1E1	457.87	-1452.61	-1678.56	314.10	1.009	0.122
214680	56637	S1E1	461.64	-1464.57	-1692.38	314.10	0.982	0.115
214680	56637	S1E1	465.33	-1476.29	-1705.92	314.10	0.944	0.197
214680	56637	S1E1	469.02	-1487.97	-1719.42	314.10	0.827	0.119
214680	56637	S1E1	472.83	-1500.06	-1733.39	314.10	0.898	0.070
214680	56637	S1E1	476.63	-1512.13	-1747.33	314.10	0.937	0.083
214680	56637	S1E1	480.57	-1524.62	-1761.77	314.10	0.913	0.058
214680	57934	S1E1	401.03	-1214.93	-1517.89	318.21	0.877	0.087
214680	57934	S1E1	405.01	-1226.99	-1532.95	318.21	0.847	0.088
214680	57934	S1E1	409.07	-1239.29	-1548.33	318.21	0.866	0.077
214680	57934	S1E1	412.94	-1251.03	-1562.99	318.21	0.914	0.112
214680	57934	S1E1	416.89	-1263.00	-1577.94	318.21	0.861	0.114
214680	57934	S1E1	420.70	-1274.52	-1592.33	318.21	0.789	0.084
214680	57934	S1E1	424.51	-1286.08	-1606.78	318.21	0.748	0.062
214680	57934	S1E1	428.40	-1297.85	-1621.49	318.21	0.796	0.059

Table 5 continued

Table 5 (*continued*)

HD	Telescope		$10^{-6}B/\lambda$	u	v	Baseline	V^2	ΔV^2
Number	MJD	Pair	(rad $^{-1}$)	(arcsec $^{-1}$)	(arcsec $^{-1}$)	(m)	(8)	(9)
(1)	(2)	(3)	(4)	(5)	(6)	(7)		
214680	57934	S1E1	432.36	-1309.85	-1636.47	318.21	0.833	0.054
214680	57934	S1E1	436.39	-1322.06	-1651.73	318.21	0.868	0.050
214680	57934	S1E1	440.56	-1334.69	-1667.51	318.21	0.889	0.055
214680	57934	S1E1	444.50	-1346.62	-1682.42	318.21	0.814	0.056
214680	57934	S1E1	448.50	-1358.77	-1697.59	318.21	0.755	0.056
214680	57934	S1E1	452.33	-1370.36	-1712.07	318.21	0.835	0.090
214680	57934	S1E1	456.09	-1381.75	-1726.30	318.21	0.900	0.077
214680	57934	S1E1	459.98	-1393.53	-1741.03	318.21	0.973	0.100
214680	57934	S1E1	463.87	-1405.32	-1755.75	318.21	1.021	0.214
214680	57934	S1E1	467.69	-1416.88	-1770.20	318.21	1.181	0.323
214680	57934	S1E1	471.43	-1428.22	-1784.36	318.21	1.196	0.307
214680	57934	S1E1	475.16	-1439.52	-1798.48	318.21	1.108	0.403
214680	57934	S1E1	479.02	-1451.22	-1813.10	318.21	0.866	0.075
214680	57934	S1E1	482.87	-1462.89	-1827.68	318.21	0.834	0.081
214680	57934	S1E1	486.86	-1474.98	-1842.78	318.21	0.808	0.055
214680	57934	S1E1	405.17	-1166.71	-1580.31	321.50	0.943	0.108
214680	57934	S1E1	409.20	-1178.30	-1596.00	321.50	0.911	0.155
214680	57934	S1E1	413.30	-1190.11	-1612.01	321.50	0.981	0.187
214680	57934	S1E1	417.21	-1201.38	-1627.28	321.50	0.902	0.103
214680	57934	S1E1	421.20	-1212.87	-1642.84	321.50	0.729	0.101
214680	57934	S1E1	425.05	-1223.94	-1657.83	321.50	0.832	0.099
214680	57934	S1E1	428.90	-1235.04	-1672.86	321.50	0.850	0.063
214680	57934	S1E1	432.83	-1246.35	-1688.18	321.50	0.907	0.087
214680	57934	S1E1	436.83	-1257.86	-1703.78	321.50	0.876	0.080
214680	57934	S1E1	440.90	-1269.59	-1719.66	321.50	0.864	0.088
214680	57934	S1E1	445.11	-1281.72	-1736.09	321.50	0.886	0.066
214680	57934	S1E1	449.09	-1293.18	-1751.61	321.50	0.905	0.094
214680	57934	S1E1	453.14	-1304.84	-1767.41	321.50	0.820	0.060
214680	57934	S1E1	457.01	-1315.97	-1782.49	321.50	0.863	0.078
214680	57934	S1E1	460.81	-1326.91	-1797.30	321.50	0.901	0.060
214680	57934	S1E1	464.74	-1338.23	-1812.63	321.50	0.875	0.072
214680	57934	S1E1	468.67	-1349.54	-1827.96	321.50	0.919	0.116
214680	57934	S1E1	472.52	-1360.65	-1843.00	321.50	1.072	0.159
214680	57934	S1E1	476.30	-1371.54	-1857.75	321.50	0.939	0.258
214680	57934	S1E1	480.07	-1382.39	-1872.45	321.50	0.861	0.259
214680	57934	S1E1	483.98	-1393.63	-1887.67	321.50	0.796	0.075
214680	57934	S1E1	487.87	-1404.84	-1902.85	321.50	0.855	0.106
214680	57934	S1E1	491.90	-1416.44	-1918.57	321.50	0.842	0.064
214680	57934	S1E1	408.36	-1113.61	-1636.91	324.04	1.016	0.134
214680	57934	S1E1	412.42	-1124.67	-1653.16	324.04	1.049	0.104
214680	57934	S1E1	416.55	-1135.95	-1669.74	324.04	1.066	0.124
214680	57934	S1E1	420.50	-1146.71	-1685.56	324.04	0.914	0.127
214680	57934	S1E1	424.52	-1157.67	-1701.68	324.04	0.814	0.242
214680	57934	S1E1	428.39	-1168.23	-1717.20	324.04	0.792	0.237
214680	57934	S1E1	432.28	-1178.83	-1732.78	324.04	0.889	0.180

Table 5 *continued*

Table 5 (*continued*)

HD	Telescope		$10^{-6}B/\lambda$	u	v	Baseline	V^2	ΔV^2
Number	MJD	Pair	(rad $^{-1}$)	(arcsec $^{-1}$)	(arcsec $^{-1}$)	(m)	(8)	(9)
(1)	(2)	(3)	(4)	(5)	(6)	(7)		
214680	57934	S1E1	436.24	-1189.62	-1748.64	324.04	0.967	0.143
214680	57934	S1E1	440.27	-1200.61	-1764.80	324.04	0.951	0.192
214680	57934	S1E1	444.37	-1211.81	-1781.25	324.04	0.977	0.261
214680	57934	S1E1	448.62	-1223.39	-1798.27	324.04	0.990	0.258
214680	57934	S1E1	452.63	-1234.32	-1814.35	324.04	0.974	0.181
214680	57934	S1E1	456.71	-1245.46	-1830.71	324.04	0.944	0.248
214680	57934	S1E1	460.61	-1256.08	-1846.33	324.04	0.980	0.294
214680	57934	S1E1	464.44	-1266.52	-1861.67	324.04	1.007	0.252
214680	57934	S1E1	468.40	-1277.32	-1877.55	324.04	0.975	0.309
214680	57934	S1E1	472.36	-1288.12	-1893.43	324.04	1.001	0.377
214680	57934	S1E1	476.24	-1298.72	-1909.01	324.04	1.123	0.464
214680	57934	S1E1	480.05	-1309.11	-1924.28	324.04	1.025	0.312
214680	57934	S1E1	483.85	-1319.47	-1939.51	324.04	0.920	0.242
214680	57934	S1E1	487.79	-1330.20	-1955.28	324.04	0.966	0.288
214680	57934	S1E1	491.71	-1340.90	-1971.00	324.04	0.988	0.269
214680	57934	S1E1	495.77	-1351.98	-1987.29	324.04	0.951	0.221
214680	57934	S1E1	412.93	-984.84	-1742.92	327.66	1.003	0.121
214680	57934	S1E1	417.03	-994.62	-1760.22	327.66	1.005	0.129
214680	57934	S1E1	421.21	-1004.59	-1777.87	327.66	0.984	0.138
214680	57934	S1E1	425.20	-1014.11	-1794.72	327.66	0.862	0.129
214680	57934	S1E1	429.26	-1023.81	-1811.88	327.66	0.712	0.120
214680	57934	S1E1	433.18	-1033.15	-1828.41	327.66	0.858	0.124
214680	57934	S1E1	437.11	-1042.52	-1844.99	327.66	0.902	0.104
214680	57934	S1E1	441.11	-1052.06	-1861.89	327.66	0.931	0.093
214680	57934	S1E1	445.19	-1061.78	-1879.09	327.66	0.935	0.088
214680	57934	S1E1	449.34	-1071.68	-1896.61	327.66	1.007	0.096
214680	57934	S1E1	453.63	-1081.92	-1914.73	327.66	0.982	0.097
214680	57934	S1E1	457.68	-1091.59	-1931.85	327.66	1.114	0.120
214680	57934	S1E1	461.81	-1101.44	-1949.27	327.66	1.246	0.153
214680	57934	S1E1	465.75	-1110.83	-1965.90	327.66	1.145	0.128
214680	57934	S1E1	469.62	-1120.07	-1982.24	327.66	1.049	0.111
214680	57934	S1E1	473.63	-1129.62	-1999.14	327.66	0.953	0.098
214680	57934	S1E1	477.63	-1139.17	-2016.05	327.66	0.805	0.092
214680	57934	S1E1	481.56	-1148.55	-2032.64	327.66	0.752	0.118
214680	57934	S1E1	485.42	-1157.74	-2048.90	327.66	0.493	0.133
214680	57934	S1E1	489.26	-1166.90	-2065.12	327.66	1.005	0.348
214680	57934	S1E1	493.24	-1176.38	-2081.90	327.66	1.086	0.158
214680	57934	S1E1	497.20	-1185.85	-2098.65	327.66	1.084	0.113
214680	57934	S1E1	501.31	-1195.64	-2115.99	327.66	1.077	0.111
214680	57934	S1E1	416.48	58.15	-2018.29	330.47	0.806	0.111
214680	57934	S1E1	420.61	58.73	-2038.33	330.47	0.865	0.154
214680	57934	S1E1	424.83	59.32	-2058.77	330.47	0.787	0.175
214680	57934	S1E1	428.85	59.88	-2078.27	330.47	0.683	0.096
214680	57934	S1E1	432.95	60.45	-2098.15	330.47	0.767	0.147
214680	57934	S1E1	436.90	61.00	-2117.29	330.47	0.721	0.122

Table 5 continued

Table 5 (*continued*)

HD	Telescope		$10^{-6}B/\lambda$	u	v	Baseline	V^2	ΔV^2
Number	MJD	Pair	(rad $^{-1}$)	(arcsec $^{-1}$)	(arcsec $^{-1}$)	(m)	(8)	(9)
(1)	(2)	(3)	(4)	(5)	(6)	(7)		
214680	57934	S1E1	440.87	61.56	-2136.49	330.47	0.734	0.064
214680	57934	S1E1	444.90	62.12	-2156.05	330.47	0.748	0.073
214680	57934	S1E1	449.01	62.69	-2175.97	330.47	0.778	0.071
214680	57934	S1E1	453.20	63.28	-2196.26	330.47	0.775	0.080
214680	57934	S1E1	457.53	63.88	-2217.24	330.47	0.760	0.034
214680	57934	S1E1	461.62	64.46	-2237.06	330.47	0.783	0.053
214680	57934	S1E1	465.78	65.04	-2257.24	330.47	0.791	0.045
214680	57934	S1E1	469.76	65.59	-2276.50	330.47	0.788	0.062
214680	57934	S1E1	473.66	66.14	-2295.42	330.47	0.706	0.053
214680	57934	S1E1	477.70	66.70	-2315.00	330.47	0.776	0.061
214680	57934	S1E1	481.74	67.26	-2334.57	330.47	0.808	0.030
214680	57934	S1E1	485.70	67.82	-2353.78	330.47	0.807	0.030
214680	57934	S1E1	489.59	68.36	-2372.61	330.47	0.871	0.038
214680	57934	S1E1	493.46	68.90	-2391.39	330.47	0.846	0.045
214680	57934	S1E1	497.48	69.46	-2410.83	330.47	0.823	0.035
214680	57934	S1E1	501.48	70.02	-2430.22	330.47	0.727	0.091
214680	57934	S1E1	505.62	70.60	-2450.30	330.47	0.779	0.090

NOTE—The complete table is provided in the on-line version.

3. STELLAR PARAMETERS

3.1. *Interferometry*

The visibility measurements we obtained for each star from our interferometric observations were fitted with a limb-darkened, single star, disk model. Linear limb-darkening coefficients in the R -band were interpolated from the tables available in Claret & Bloemen (2011) using the stellar parameters given in Table 1. These limb darkening coefficients were calculated for model atmospheres that adopt a solar metallicity and a microturbulent velocity of 2 km s^{-1} , and they were derived to maintain flux conservation. **The effect of limb-darkening is minimal in O-type stars and any uncertainty in the fitted size due to uncertainty in the adopted limb-darkening coefficient will be much smaller than our other sources of uncertainty discussed below.** Figures 1 and 2 show the visibility measurements for each star plus an error-weighted fit of all the data with a limb-darkened disk model. Table 6 lists the derived uniform disk (UD) and limb-darkened (LD) disk angular diameters θ , the latter calculated for a linear limb-darkening coefficient μ .

The fitting scheme assigned an uncertainty to the angular diameter based upon the size of the residuals to the fit. However, multiple-night observations of stellar diameters with PAVO show an external night-to-night

scatter that is larger than indicated by the uncertainty from measurements within a night by about 5% (Maestro et al. 2013). We checked this inter-night variation with larger sample of 25 B stars observed with the CHARA Array (to be presented in a forthcoming paper) and found the average error to be consistent with the 5% quoted by Maestro et al. (2013) for PAVO data. Thus, we have applied a 5% night-to-night scatter to our error budget. The other source of uncertainty is related to the diameters of the calibrator stars. Because some of our targets are very small (only 0.11 mas for 10 Lac), the calibrator stars may have sizes comparable to the targets. These calibrators can still be used in the analysis but the error in their sizes will play a much bigger role in the error budget than is usually the case where the calibrators are much smaller than the corresponding targets. To account for this effect we fit the data for each star after adjusting the calibrator sizes by plus and minus one sigma, and then derived the range in the solutions. The final uncertainties given in Table 6 are the quadratic sum of the uncertainties from the internal fit uncertainties, the night-to-night external error and the half-range from varying the calibrator size.

The observations from different nights were not averaged for ζ Oph as there is a true physical difference in size measured along different baselines due to the star’s rotational distortion. The results in Table 6 show that the angular size varies by 15% between the S2W1 and

Table 6. Angular Diameters

Star	Telescope		θ_{UD}		θ_{LD}	$\theta_{LD}(\text{U79})$	$\theta_{LD}(\text{HB74})$	$\theta_{LD}(\text{CADARS})$	$\theta_{LD}(T_{\text{eff}})$
Name	Pair	N_{V^2}	(mas)	μ	(mas)	(mas)	(mas)	(mas)	(mas)
ξ Per	W1E1	23	0.216 ± 0.016	0.174	0.218 ± 0.016^1	0.26	0.245 ± 0.010
α Cam	S1E1	23	0.250 ± 0.014	0.250	0.256 ± 0.014^1	0.292 ± 0.003	...	0.29	0.245 ± 0.010
λ Ori A	S1E1,W1E1	168	0.219 ± 0.015	0.253	0.226 ± 0.015	0.235 ± 0.003	...	0.24	0.228 ± 0.009
ζ Ori A	W1E1	23	0.546 ± 0.029	0.203	0.556 ± 0.029^1	0.527 ± 0.010	0.48 ± 0.04	0.47	0.485 ± 0.019
ζ Oph	S2W1	69	0.454 ± 0.010	0.204	0.462 ± 0.010	0.494 ± 0.003	0.51 ± 0.05	0.54	0.539 ± 0.021
	S2E2	161	0.532 ± 0.010	0.204	0.540 ± 0.010				
10 Lac	S1E1	119	0.11 ± 0.02	0.183	0.11 ± 0.02	0.123 ± 0.002	...	0.13	0.121 ± 0.005

NOTE—¹ θ_{LD} represents preliminary results that are based upon only a single data bracket. N_{V^2} = number of visibility measurements. U79 = [Underhill et al. \(1979\)](#), HB74 = [Hanbury Brown et al. \(1974\)](#), CADARS = [Pasinetti Fracassini et al. \(2001\)](#), T_{eff} = diameter derived from temperature and SED.

S2E2 baselines. Below in Section 4.1 we present an ellipsoidal fit of the angular diameter as a function of position angle.

3.2. Spectrophotometry

The goal of our spectrophotometric analysis was to compare our results from directly measured angular sizes and observed spectra to predictions of parameters from a stellar atmospheric model. Given the spectral flux across a wavelength range and an estimate of the stellar effective temperature T_{eff} from spectral line studies, the models can predict what the angular size should be. We can then compare this against our interferometrically determined angular sizes to test the consistency of model line and flux predictions.

We used fluxes from multiple sources for our targets to create spectral energy distributions (SEDs) that span the wavelength range from ultraviolet to infrared. Sources used for each part of the spectrum are given in Table 7. Ultraviolet spectra obtained from the *International Ultraviolet Explorer* satellite were recalibrated with a routine by [Massa & Fitzpatrick \(2000\)](#) to correct the flux values. Longer wavelength infrared fluxes were omitted for the supergiant and giant O stars because their winds create an excess flux in the far infrared that is absent from models without winds. We rebinned the UV and optical spectra to a low resolving power of $R = \lambda/\Delta\lambda = 60$ on a $\log \lambda$ grid in order to better balance the sampling across the whole spectrum. All flux values in the spectra were assigned a uniform 3% error to ensure our fitting program fit all points equally and did not give more weight to any one part of the spectrum. The exception to this was the case of 10 Lac, a target which has very good data available in the ultraviolet and optical from HST/STIS ([Bohlin et al. 2017](#)).

The errors on these flux values were lower than 3% and the original error values were used for the fitting.

The spectra were compared to the TLUSTY OSTAR2002 stellar atmosphere models that adopt solar metallicity and a microturbulent velocity of 10 km s^{-1} ([Hubeny & Lanz 1995](#); [Lanz & Hubeny 2003](#)). Our fitting routine used a grid search method to fit the SED using three parameters: limb-darkened angular size (θ_{LD}), effective temperature (T_{eff}), and reddening ($E(B-V)$). For any given set of parameters, a spectrum was extracted from the O star grid through interpolation in T_{eff} and $\log g$ (the latter from the adopted gravity given in Table 1). The model spectrum was rebinned to $R = 60$ in the same way as the observed SED, and then the fluxes were attenuated for interstellar extinction using the IDL Code *fmrcurve.pro* for a ratio of total-to-selective extinction of 3.1 ([Fitzpatrick 1999](#)). Adopting an R value greater than 3.1 would result in the model fit predicting a larger angular diameter. Recent extinction fits by [Maíz Apellániz & Barbá \(2018\)](#) give an R value close to 3.1 for all our stars with the exception of α Cam with an $R = 4.0$. Finally the model spectra were rescaled according to the assumed angular diameter and interpolated to the observed wavelength points for direct comparison with the observed SED.

In cases where there is a close, bright companion (Table 3), the extra flux from the companion was included in our fitting. The effective temperature and surface gravity of the companion were used to calculate a model companion spectrum in the same way as above using either the TLUSTY OSTAR2002 ([Lanz & Hubeny 2003](#)) or BSTAR2006 models ([Lanz & Hubeny 2007](#)), depending on the temperature of the companion. The companion flux was then rescaled according to the V -band magnitude difference Δm_V (Table 3) and added to the

Table 7. Spectrophotometry Sources

Star	Far UV	Near UV	Optical	IR
ξ Per	SWP45474	LWP23809	SP1	2MASS
α Cam	HUT	LWP17592	SP2	2MASS
λ Ori A	OAO	OAO	SP1	2MASS
ζ Ori A	SWP33049, SWP33050	LWP11671, LWP12826	SP3	2MASS
ζ Oph	SWP06776, SWP18252	LWP12637, LWR14381	SP1	2MASS, WISE, AKARI, Spitzer, IRAS
10 Lac	SWP*+STIS	HST/STIS	HST/STIS	2MASS, WISE, AKARI, IRAS

NOTE—The UV spectra are primarily from the archive of the *International Ultraviolet Explorer* (low dispersion, large aperture) where the file number is related to the camera: SWP = Short Wavelength Prime, LWP = Long Wavelength Prime, and LWR = Long Wavelength Redundant. SWP* refers to the average of 52 SWP spectra covering the 1160 – 1646 Å range. All the fluxes were corrected using the algorithm from Massa & Fitzpatrick (2000). Other UV fluxes are from HUT = Hopkins Ultraviolet Telescope (Buss et al. 1995), OAO = Orbiting Astronomical Observatory 2 (Code & Meade 1979), and HST/STIS from the CALSPEC database (Bohlin et al. 2017). Optical spectrophotometry sources are coded as SP1 = Burnashev (1985), SP2 = Kharitonov et al. (1988), and SP3 = Krisciunas et al. (2017). IR fluxes are from 2MASS (Cutri et al. 2003), WISE (Cutri et al. 2012), AKARI (Ishihara et al. 2010), Spitzer (Ardila et al. 2010), and IRAS (Helou & Walker 1988).

model flux calculated for the primary. This combined flux spectrum was then used for spectrophotometric fitting of the observed SED.

We began the SED modeling process by creating a grid of angular size and effective temperature, the latter over a range and step size chosen to match the models in the TLUSTY grid. For each pair of θ and T_{eff} , models were calculated over a grid of reddening values, and the best fit $E(B - V)$ was found by making a parabolic fit around the reddening grid point with the lowest value of reduced χ^2_{ν} . The best-fit $E(B - V)$ and χ^2_{ν} values were stored in matrices as functions of θ_{LD} and T_{eff} .

Contour maps were created by plotting the χ^2_{ν} matrix for each star, and these are shown in Figure 3. Overplotted as vertical lines are the angular size obtained from our interferometry with 1σ error margins, and horizontal lines show the average literature temperature from Table 1 with 1σ error margins. The shape of the contours shows that there is generally a valley of low χ^2_{ν} where the effective temperature has an inverse square dependence on angular size as expected from our discussion in Section 1. The contours for the best-fit $E(B - V)$ values (not shown) are parallel lines that follow the curve of the minimum in χ^2_{ν} space. Therefore, any temperature and angular size combination chosen along the minimum valley will have a very similar associated $E(B - V)$ value.

We first consider what angular size is predicted from the χ^2_{ν} diagrams for estimates of T_{eff} from published studies of the line spectra (Table 1). We examined the horizontal line associated with the average literature temperature for each star, and we found the angular size where the line crossed the minimum χ^2_{ν} . The derived angular sizes for these best fits are listed in the final column of Table 6 under the heading $\theta_{LD}(T_{\text{eff}})$. A

comparison of our interferometric angular size and the model predicted size is shown in Figure 5 and discussed in Section 4.2. We assume for simplicity that there is a 4% uncertainty associated with $\theta_{LD}(T_{\text{eff}})$, which is an approximate estimate based upon flux uncertainties of 3%, reddening uncertainties of 2%, and line-based temperature uncertainties of 3%.

We next consider estimates for effective temperature and reddening that rely on the observed interferometric sizes and the χ^2_{ν} the contour plots. We followed the vertical line along the value of our observed angular size and found the temperature where the lowest χ^2_{ν} was attained (marked by a diamond symbol). These interferometrically determined temperatures and the associated reddening estimates are given in Table 8, along with comparisons to previously determined values. The range in acceptable values of T_{eff} can be large because the fractional errors in temperature are about twice as large as the fractional errors in angular size (which may be significant).

The spectral energy distributions (SED) and the model best fits are shown in Figure 4. The symbols represent the observed spectral data while the solid green line shows the model SED for our interferometric size and best fit temperature and reddening. For comparison, the dashed line (often overlapping the solid line) shows the model SED based on the literature temperature and the angular size corresponding to the local minimum of the χ^2_{ν} contours.

4. DISCUSSION

4.1. Notes on Individual Stars

ξ Per (HD 24912) is one of three O-type runaway stars in the list (along with α Cam and ζ Oph), and these are

Table 8. Effective Temperature and Reddening Estimates

Star	T_{eff} (Best Fit)	T_{eff} (Literature)	$E(B - V)^a$	$E(B - V)^b$	$E(B - V)^c$
Name	(kK)	(kK)	(mag)	(mag)	(mag)
ξ Per	<40	34.3 ± 0.8	0.291	0.25	0.278 ± 0.007
α Cam	28.0 ± 1.5	29.4 ± 1.0	0.298	0.26	0.262 ± 0.006
λ Ori A	36.0 ± 0.9	34.5 ± 0.8	0.107	0.12	0.177 ± 0.011
ζ Ori A	<28	29.5 ± 1.0	0.067	0.08	0.044 ± 0.007
ζ Oph	33.5 ± 1.3	32.1 ± 1.3	0.350	0.29	0.297 ± 0.006
10 Lac	40.0 ± 1.3	35.5 ± 0.5	0.096	0.08	0.077 ± 0.006

NOTE— $E(B - V)$ estimates: a. Best fit, b. Savage et al. (1977), c. Maíz Apellániz & Barbá (2018).

Table 9. Distance and Radius Estimates

Star	d_1	d_2	d_3	d_4	d_5	d_6	R_{GAIA}	$\langle d \rangle$	R
Name	(pc)	(pc)	(pc)	(pc)	(pc)	(pc)	(R_{\odot})	(pc)	(R_{\odot})
ξ Per	398	...	486 ± 57	416 ± 158	433 ± 46	10.1 ± 1.3
α Cam	1010	1175 ± 118	1607 ± 275	...	821	731 ± 175	20.1 ± 4.9	1068 ± 346	29.4 ± 9.7
λ Ori A	501	398 ± 40	...	361 ± 90	438	417 ± 10	10.0 ± 0.6	423 ± 51	10.2 ± 1.3
ζ Ori A	501	350 ± 35	297 ± 45	239 ± 48	391	381 ± 10	22.8 ± 1.3	359 ± 89	21.5 ± 5.4
ζ Oph	154	188 ± 19	222 ± 22	112 ± 11	145	172 ± 31	$8.5 - 10.0$	165 ± 37	$8.9 - 10.5$
10 Lac	603	631 ± 63	579 ± 76	542 ± 108	...	478 ± 10	5.7 ± 1.0	566 ± 59	6.7 ± 1.4

NOTE—Distance references: 1. Shull & van Steenberg (1985), 2. Underhill et al. (1979), 3. Megier et al. (2009), 4. van Leeuwen (2007) and Maíz Apellániz et al. (2008), 5. de Zeeuw et al. (1999) and Kharchenko et al. (2005), 6. Gaia Collaboration et al. (2018).

usually single stars (Gies & Bolton 1986). The observed angular size is smaller than expected (Table 6; Fig. 3), however, given that the measurements are preliminary and that the minimum χ^2_{ν} lies at a diameter only 1.4σ larger than measured, we do not consider the difference significant. The χ^2_{ν} minimum valley has a steep slope in Figure 3, so the derived uncertainty in T_{eff} is large and we list only an upper limit in Table 8.

α Cam (HD 30614) presents a case where the observed angular size is somewhat larger than expected **from model predictions** (Table 6), but θ_{LD} and $\theta_{LD}(T_{\text{eff}})$ agree within the uncertainties.

λ Ori A (HD 36861) represents an example with excellent agreement between θ_{LD} and $\theta_{LD}(T_{\text{eff}})$ (Table 6). During the data analysis one of the stars used as a calibrator, HD 35149, was found to be a binary and was thus rejected from the calibration process. The final data for λ Ori A are calibrated with only one calibrator star, and the visibilities are slightly more noisy than otherwise expected.

ζ Ori A (HD 37742) has a larger angular size than expected **from model predictions** (Table 6; Fig. 3).

The star is the brightest component Aa of a triple system with a close companion Ab, which had a predicted separation of 33 mas at the time of our observations (Hummel et al. 2013). The light from this companion will affect the spectrum and the visibility curve of ζ Ori A, and we accounted for the extra flux of the companion for both the fits of the visibilities and the SED (Section 2). We calculated a binary model for the visibilities, shown in Figure 2, using the predicted position angle, separation, and radius ratio $R/R_{\odot} = 0.365$ given by Hummel et al. (2013). The model shows fast and low amplitude oscillations of the visibility curve that are roughly consistent with the observations, and the binary fit yields $\theta_{LD} = 0.556 \pm 0.029$ mas. ζ Ori A was recently observed with the FRIEND beam combiner at the CHARA Array (M.-A. Martinod, private communication) yielding angular diameters of 0.54 ± 0.01 and 0.45 ± 0.12 mas for Aa and Ab, respectively. Their angular diameter measurement agrees within errors with ours for ζ Ori Aa. The estimate of T_{eff} associated with the observed angular diameter attains a χ^2_{ν} minimum at the lower boundary of

the OSTAR2002 grid (Fig. 3), so only an approximate upper limit is given in Table 8.

ζ Oph (HD 149757) is a well-known, rapidly rotating star. According to the analysis by Howarth & Smith (2001), the star has an equatorial, angular rotational velocity that is 90% of the critical value, and it is viewed in an equatorial orientation with a spin inclination axis angle of 70°. Consequently, its shape should appear oblate due to its rapid rotation. We observed ζ Oph on different baselines with different position angles (S2W1 at $-42^\circ.8$ and S2E2 at $17^\circ.9$) to measure directly this deviation from a perfect sphere. Our measurements are insufficient to make a full ellipsoidal model of the size variation, but we can make a restricted fit by setting the position angle of the rotational axis from earlier polarimetric work. ζ Oph sometimes appears as a Oe star with H Balmer line emission from a circumstellar disk. At the times of observation (July 2016 and June 2017), it did not show H α emission in its spectra, so it is reasonable to assume that any disk gas has dissipated and we are measuring the angular size of the star itself. However, during a past epoch when a disk was present, Poeckert et al. (1979) used spectropolarimetry to determine the position angle of the disk minor axis as 132.5 ± 6.0 deg east from north. We assume that the circumstellar disk axis is parallel to the stellar rotation axis, so that this is also the position angle of the projected minor axis of the star's shape. We made a fit of the limb-darkened angular diameter for each V^2 measurement, and then we fit an ellipsoid to the diameter as a function of position angle in the sky with the position angle of the minor axis set from the spectropolarimetric result. This gives a major axis of 0.56 mas and a minor axis of 0.48 mas. The fitted ellipse is shown in Figure 6. The ratio of minor to major axis of 0.86 is similar to the polar to equatorial radius ratio of $7.5R_\odot/9.1R_\odot = 0.82$ found by Howarth & Smith (2001), although the absolute radii we find are slightly larger because we adopt a larger distance (Table 9). This star is a good target for future interferometric imaging to determine better the rotational distortion and the associated gravity and limb darkening (Che et al. 2011). ζ Oph is a runaway star that may have been launched from a supernova explosion in a binary. Its path has been traced back with that of a pulsar that was ejected during the supernova (Hoogerwerf et al. 2000).

10 Lac (HD 214680) has the smallest angular diameter ($\theta_{LD} = 0.11 \pm 0.02$ mas) that has been measured with CHARA to date. Because this is below the nominal resolution limit of PAVO of 0.2 mas, we need to check carefully the associated uncertainty of our measurement. Three calibrators were used for the observa-

tions of 10 Lac. The fitted angular size is very sensitive to the error in the calibrator size when the target star is smaller in angular size than the calibrator, as in this case. To account for this, we varied each calibrator in size by plus and minus one sigma, then refit the data with the new calibrator size. We then took the range between the fits as part of our error budget. This method was subsequently applied to all stars in the sample (Section 3.1). Working close to the resolution limit of PAVO resulted in some non-physical ($V^2 > 1$) visibility estimates. We retained these points except in one case where an entire bracket yielded visibilities greater than unity. Both spectroscopic observations and our interferometric results arrive at relatively high effective temperatures, 40.0 kK and 35.5 kK, respectively, that are well above the 31.9 kK temperature associated with its classification of O9 V (Martins et al. 2005). It has been noted in other studies (Simón-Díaz et al. 2014; Holgado et al. 2018) that the T_{eff} values from the calibrations in Martins et al. (2005) are too low for O9 V stars. However, the extended minimum valley in the χ^2_ν diagram (Fig. 3) does encompass the lower temperature (as does the uncertainty region of measured angular diameter).

4.2. Consistency with SED Fits from Model Atmospheres

Our primary goal was to test whether the angular diameters, spectroscopically determined temperatures, and spectral energy distributions (SEDs) led to a consistent set of stellar parameters. If so, then the intersection of the observed angular diameter (vertical lines) and estimated effective temperature (horizontal line) would cross near the minimum χ^2_ν contours in Figure 3. We find that the angular diameters estimated from the published effective temperatures and fits of the SEDs ($\theta_{LD}(T_{\text{eff}})$ given in the final column of Table 6) are generally in good agreement with the interferometric angular diameters. A comparison of observed θ_{LD} and the predicted angular size $\theta_{LD}(T_{\text{eff}})$ is shown in Figure 5. This figure shows that the average ratio of $\theta_{LD}(T_{\text{eff}})$ to θ_{LD} is approximately 0.99 ± 0.03 . Note that the three stars with the greatest discrepancy in angular size are ξ Per, ζ Ori A, and ζ Oph. However, the results for the first two of these stars, ξ Per and ζ Ori A, are preliminary because the diameters are based upon one data bracket. ζ Oph is rotationally distorted, so gravity darkening will complicate the meaning of θ_{LD} and the comparison to a model predicted size may not be entirely valid. The targets with many observations, λ Ori A and 10 Lac, show good agreement between the interferometric and spectroscopically derived angular diameters.

We can use the angular size and distance to obtain the stellar radius. In Table 9 we list distance estimates from six sources. The columns labeled by d_1 and d_2 give distances based upon a calibration of absolute magnitude and spectral classification from Shull & van Steenberg (1985) and Underhill et al. (1979), respectively. The next estimate d_3 is based upon the interstellar Ca II line strengths (Megier et al. 2009). The fourth estimate d_4 is derived from the *Hipparcos* parallax (van Leeuwen 2007) with a correction term for the Lutz-Kelker bias (Maíz Apellániz et al. 2008). The next estimate d_5 is the distance to the host cluster (Kharchenko et al. 2005) or association (de Zeeuw et al. 1999) if the target is a known member. The final value d_6 is derived from the parallaxes from Gaia DR2 (Gaia Collaboration et al. 2018). **The DR2 coverage is incomplete for bright stars (no measurements for ξ Per and ζ Ori A) and the errors are relatively large and probably underestimated (Luri et al. 2018).** Consequently, we adopted the parallax of fainter, physical companions whenever possible. The DR2 parallaxes for λ Ori A, B have large errors, so we adopted the mean of the parallaxes for components C and D. There is no parallax given for ζ Ori A, so we used the listing for the C component. We applied the parallax of component B for 10 Lac, because of the much larger error associated with component A. **There was no faint companion available to use for α Cam, so the formal Gaia DR2 parallax error is large.** The third to last and final columns give the stellar radius corresponding to the Gaia (column 7) and mean distance (column 9), respectively, as derived from our angular size measurements (Table 6). Note that the standard deviation of the mean distance may underestimate the total uncertainty if some subsets rely upon the same spectroscopic calibration of spectral type and M_V . The radius range listed for ζ Oph (HD 149757) relates to the smaller and larger angular sizes found at different position angles. The derived radii generally agree within the range associated with their spectral classifications as given by Martins et al. (2005), except for the two giants, ξ Per and λ Ori A, which have radii closer to those of main sequence stars.

Our interferometric survey of O-star diameters yields results that are comparable to the expected diameters based upon the published temperatures and model fits of the SED (Table 6; Fig. 5), except in the cases of two evolved stars, ξ Per and ζ Ori A, where our data coverage is quite limited. Additional interferometric observations are needed to confirm the smaller and larger diameters found in these two cases, respectively. There are several possible explanations for such discrepancies.

First, it is possible that some of our calibrator stars have yet undetected binary companions. If such companions added incoherent flux to the visibility measurements, then the calibrator visibilities would be depressed and we would infer smaller diameters for the targets. Additional observations with different calibrators would test this idea. Secondly, it is possible that the quoted diameters of the calibrators have larger than expected uncertainties. The JSDC diameter estimates (Chelli et al. 2016) rely on relations based upon colors and spectral classification that are set by measured angular sizes. However, there are relatively few measurements among the B-type and early A-type stars that form our set of calibrators (Table 4), so the relations may need more thorough testing.

Finally, it is possible that the model atmospheres that we used to fit the SEDs underestimate or overestimate the flux over the observed range (1200 Å to 2 μ m), so that the angular diameters inferred from the SED fits are too large or small, respectively. All our fits rely on the TLUSTY grid of models (Lanz & Hubeny 2003) that assume a plane-parallel geometry and that neglect stellar winds. We made a spot check of the models against the predictions of the non-LTE code CMFGEN (Hillier & Miller 1998) that can account for spherical geometry and outflows. The initial comparison was made assuming $T_{\text{eff}} = 34.4$ kK, $\log g = 3.5$, solar abundances, and a microturbulent velocity of 10 km s $^{-1}$. A comparison of the predicted fluxes between a plane-parallel model from CMFGEN and one from TLUSTY showed better than 1% agreement in flux ratio over the observed range. This confirms earlier results showing excellent agreement between TLUSTY and CMFGEN (Hillier & Lanz 2001). Additional tests indicated that the mean flux over the observed range was about 1% higher for a CMFGEN spherical model with wind loss and was about 2% higher in models with the microturbulent velocity increased to 20 km s $^{-1}$. Thus, while model differences may account for angular size discrepancies of a few percent, the larger difference seen in the supergiant ζ Ori A may require other explanations. Interferometric observations at longer wavelengths would help test models that include winds, because of the increasing proportion of wind flux into the IR-regime. We will extend this investigation in a subsequent paper to the cooler B-type stars to further explore the differences between interferometrically and spectroscopically determined parameters for massive stars.

This work is based upon observations obtained with the Georgia State University Center for High Angular Resolution Astronomy Array at Mount Wilson Observa-

tory. The CHARA Array is supported by the National Science Foundation under Grant No. AST-1211929, AST-1411654, AST-1636624, and AST-1715788. Institutional support has been provided from the GSU College of Arts and Sciences and the GSU Office of the Vice President for Research and Economic Development. KDG expresses her thanks for the financial support of a NASA Georgia Space Grant Fellowship. This research has made use of the Jean-Marie Mariotti Center JSDC catalog, the VizieR catalogue access tool and SIMBAD database (CDS, Strasbourg, France), and data from the European Space Agency (ESA) mission *Gaia* (<https://www.cosmos.esa.int/gaia>), processed by the *Gaia* Data Processing and Analysis Consortium (DPAC, <https://www.cosmos.esa.int/web/gaia/dpac/consortium>). Funding for the DPAC has been provided by national institutions, in particular the institutions participating in the *Gaia* Multilateral Agreement.

Software: TLUSTY (Hubeny & Lanz 1995; Lanz & Hubeny 2003, 2007), CMFGEN (Hillier & Miller 1998)

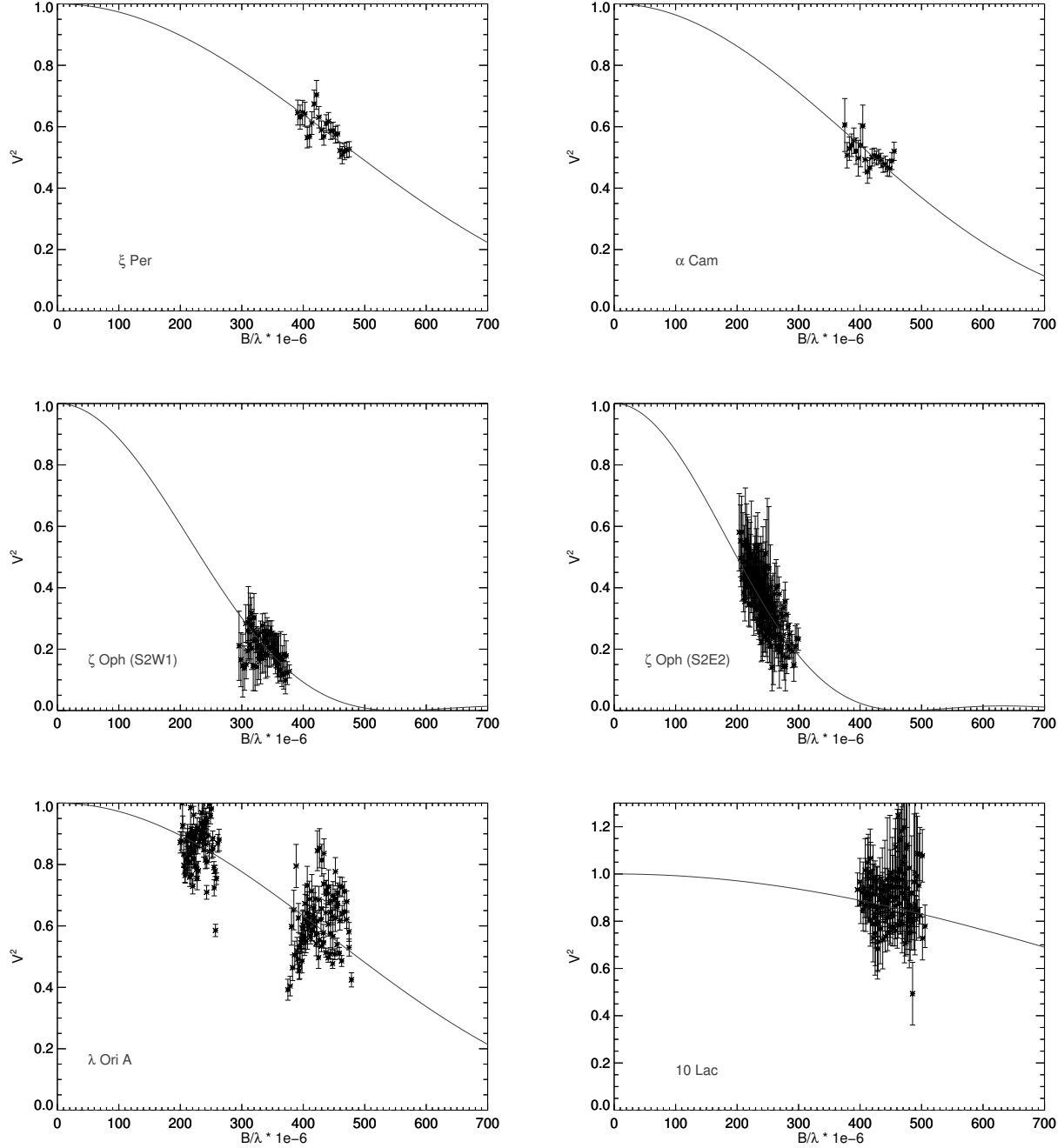


Figure 1. Squared visibility versus spatial frequency for five target stars. The solid line indicates the best fit for a single star limb-darkened disk model.

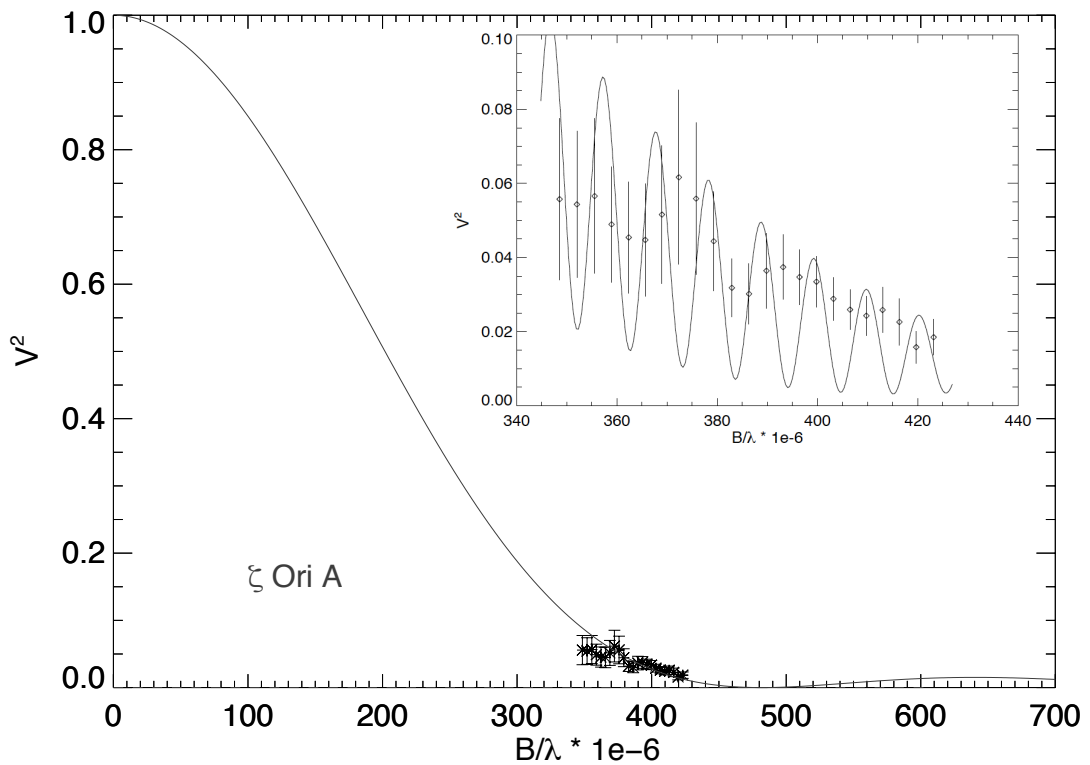


Figure 2. Visibility measurements for ζ Ori A with the solid line showing an error weighted single star fit. An error weighted binary fit to the visibility data is shown inset.

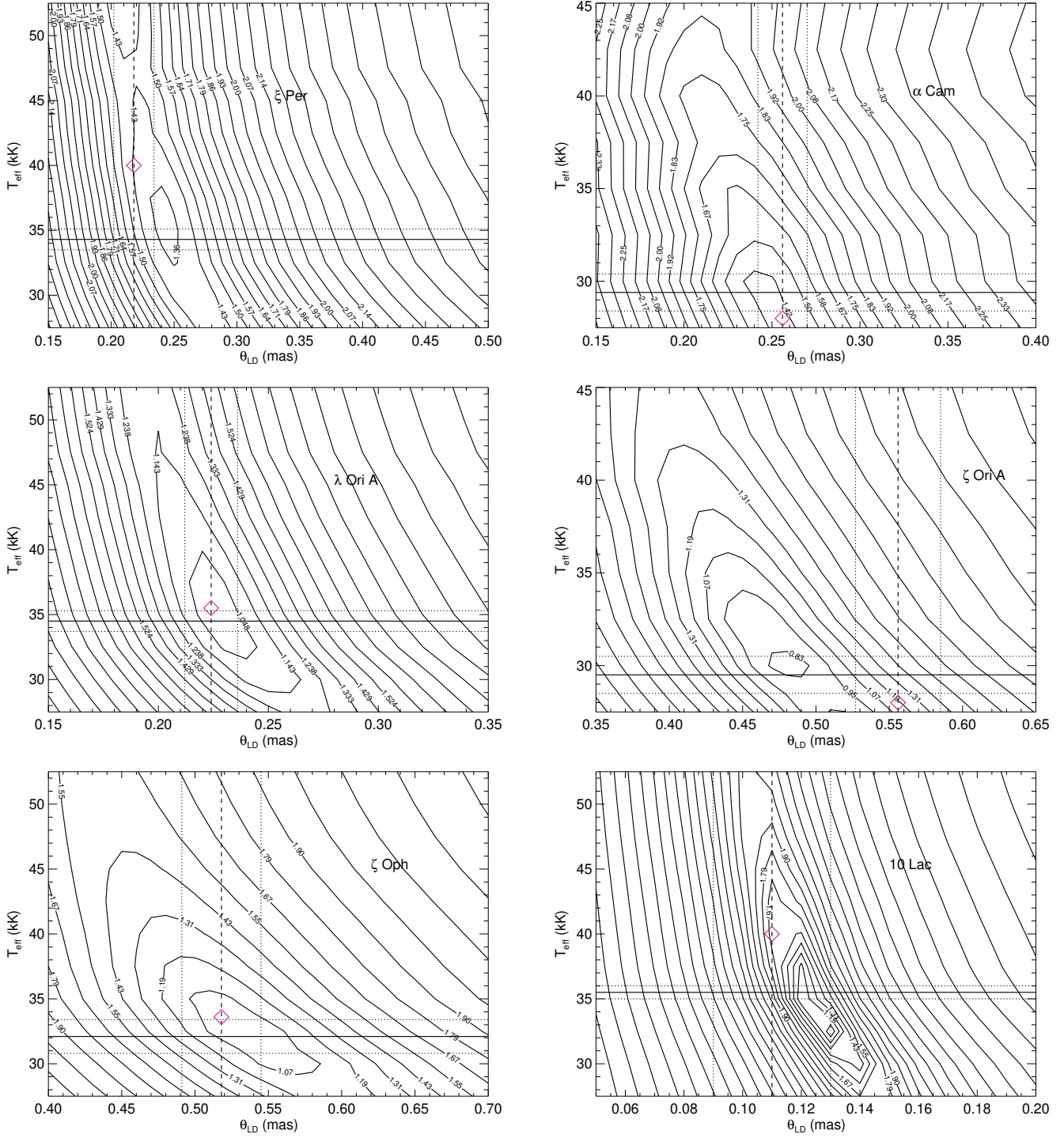


Figure 3. Contour maps of the χ^2 differences between fitted TLUSTY stellar atmosphere model and observed spectra for each star. Contours are drawn at equal intervals of $\Delta\chi^2$. Overplotted are vertical lines showing angular size obtained from our interferometry and horizontal lines showing the average literature temperature. Dotted lines show an error margin of 1σ for the angular size and temperature. Diamonds indicate the best fit model temperature for our directly determined angular size.

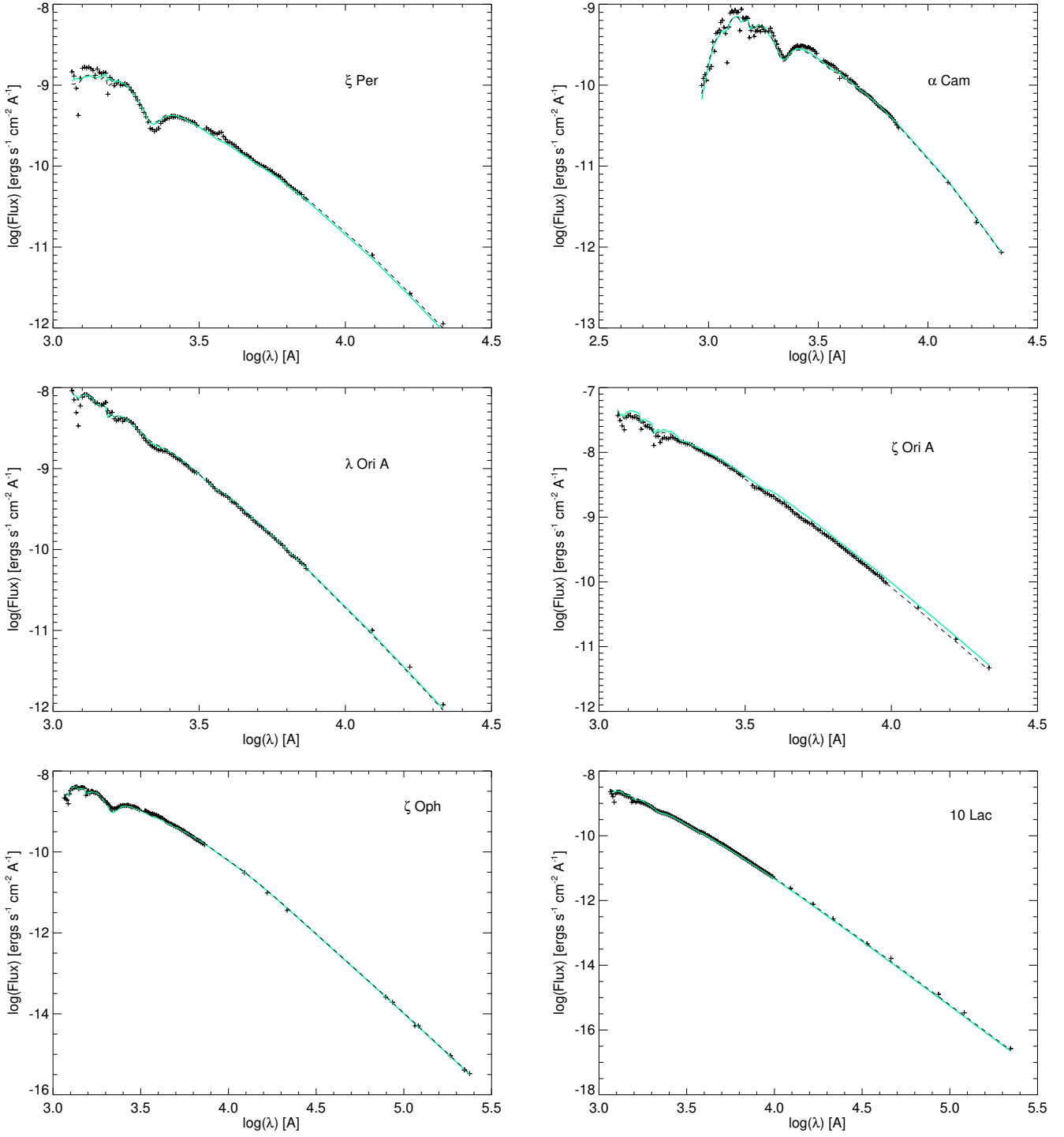


Figure 4. Spectral energy distributions for targets stars with the best fit model shown in the solid green line. Best fit models were chosen using our observed angular diameter from interferometry combined with the best fit temperatures and reddening values found from our contour maps (Fig. 3). The dashed line indicates the SED derived by setting the average published T_{eff} and determining the best fit angular size $\theta_{LD}(T_{\text{eff}})$.

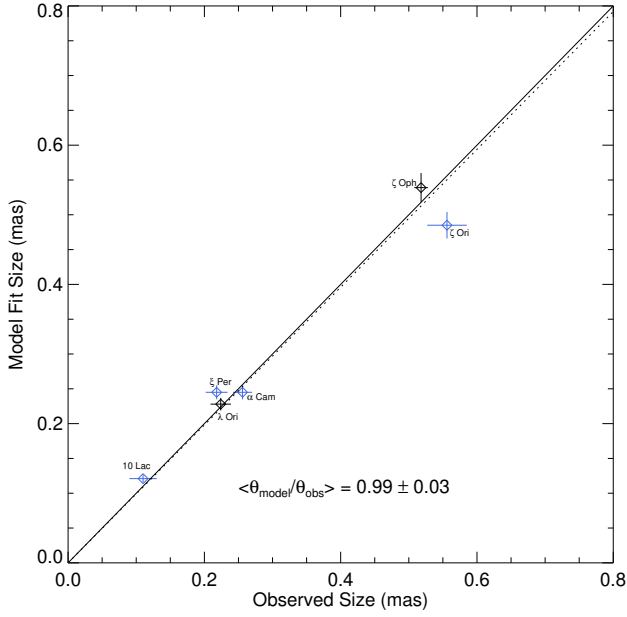


Figure 5. Observed angular size θ_{LD} compared to the angular size $\theta_{LD}(T_{\text{eff}})$ derived from the published T_{eff} and fit to the SED. The solid line shows a line with a slope of unity for reference, and the dashed line shows the trend for the mean ratio of these diameters. Blue points indicate diameter estimates based upon only a single data bracket or an extremely small angular size in the case of 10 Lac.

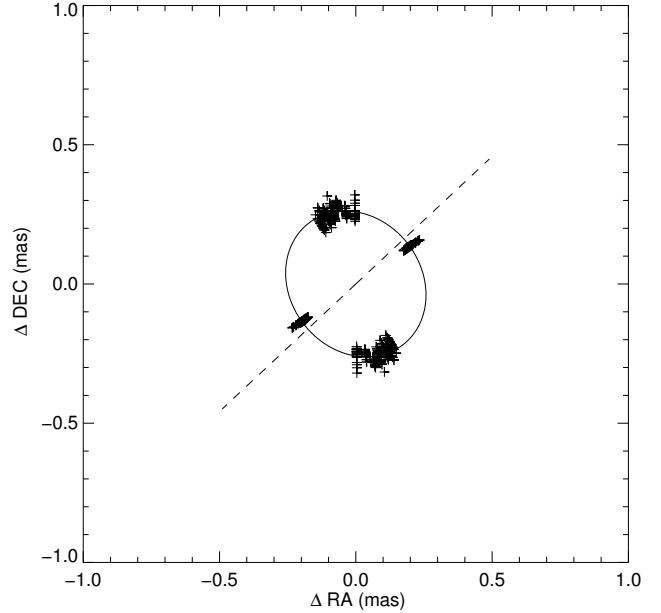


Figure 6. A simple ellipse fitted to our interferometric data for ζ Oph. Each symbol shows the derived angular size of a limb-darkened star whose visibility equals the observed value, and each is plotted at a position angle derived from the (u, v) spatial frequencies of the observation. The fit was made of the major and minor axes with the position angle of the minor axis set by published polarimetry. The dashed line shows the adopted rotational axis of the star at a position angle of $132^{\circ}5$.

REFERENCES

- Abbott, D. C., & Hummer, D. G. 1985, *ApJ*, 294, 286
- Ardila, D. R., Van Dyk, S. D., Makowiecki, W., et al. 2010, *ApJS*, 191, 301
- Bohlin, R. C., Mészáros, S., Fleming, S. W., et al. 2017, *AJ*, 153, 234
- Bouret, J.-C., Donati, J.-F., Martins, F., et al. 2008, *MNRAS*, 389, 75
- Bourg  s, L., Lafrasse, S., Mella, G., et al. 2014, in Astronomical Society of the Pacific Conference Series, Vol. 485, Astronomical Data Analysis Software and Systems XXIII, ed. N. Manset & P. Forshay (San Francisco: ASP), 223
- Burnashev, V. I. 1985, Abastumanskaia Astrofizicheskaiia Observatoriia Byulleten, 59, 83
- Buss, Jr., R. H., Kruk, J. W., & Ferguson, H. C. 1995, *ApJL*, 454, L55
- Che, X., Monnier, J. D., Zhao, M., et al. 2011, *ApJ*, 732, 68
- Chelli, A., Duvert, G., Bourg  s, L., et al. 2016, *A&A*, 589, A112
- Claret, A., & Bloemen, S. 2011, *A&A*, 529, A75
- Code, A. D., Bless, R. C., Davis, J., & Brown, R. H. 1976, *ApJ*, 203, 417
- Code, A. D., & Meade, M. R. 1979, *ApJS*, 39, 195
- Cutri, R. M., Skrutskie, M. F., van Dyk, S., et al. 2003, 2MASS All Sky Catalog of point sources.
- Cutri, R. M., Wright, E. L., Conrow, T., et al. 2012, Explanatory Supplement to the WISE All-Sky Data Release Products, Tech. rep.
- de Zeeuw, P. T., Hoogerwerf, R., de Bruijne, J. H. J., Brown, A. G. A., & Blaauw, A. 1999, *AJ*, 117, 354
- Fitzpatrick, E. L. 1999, *PASP*, 111, 63
- Gaia Collaboration, Brown, A. G. A., Vallenari, A., et al. 2018, *A&A*, 616, A1
- Gies, D. R., & Bolton, C. T. 1986, *ApJS*, 61, 419
- Hanbury Brown, R., Davis, J., & Allen, L. R. 1974, *MNRAS*, 167, 121
- Helou, G., & Walker, D. W. 1988, in Infrared astronomical satellite (IRAS) catalogs and atlases. Volume 7, p.1-265, Vol. 7
- Herrero, A., Puls, J., & Najarro, F. 2002, *A&A*, 396, 949
- Hillier, D. J., & Lanz, T. 2001, in Astronomical Society of the Pacific Conference Series, Vol. 247, Spectroscopic Challenges of Photoionized Plasmas, ed. G. Ferland & D. W. Savin (San Francisco: ASP), 343
- Hillier, D. J., & Miller, D. L. 1998, *ApJ*, 496, 407
- Holgado, G., Sim  n-D  az, S., Barb  , R. H., et al. 2018, *A&A*, 613, A65
- Hoogerwerf, R., de Bruijne, J. H. J., & de Zeeuw, P. T. 2000, *ApJL*, 544, L133
- Howarth, I. D., & Smith, K. C. 2001, *MNRAS*, 327, 353
- Hubeny, I., & Lanz, T. 1995, *ApJ*, 439, 875
- Hummel, C. A., Rivinius, T., Nieva, M.-F., et al. 2013, *A&A*, 554, A52
- Hummer, D. G., Abbott, D. C., Voels, S. A., & Bohannan, B. 1988, *ApJ*, 328, 704
- Ireland, M. J., M  rand, A., ten Brummelaar, T. A., et al. 2008, in Proc. SPIE, Vol. 7013, Optical and Infrared Interferometry, 701324
- Ishihara, D., Onaka, T., Kataza, H., et al. 2010, *A&A*, 514
- Kharchenko, N. V., Piskunov, A. E., R  ser, S., Schilbach, E., & Scholz, R.-D. 2005, *A&A*, 438, 1163
- Kharitonov, A. V., Tereshchenko, V. M., & Knjazeva, L. N. 1988, The spectrophotometric catalogue of stars (Alma Ata: Nauka)
- Krisciunas, K., Suntzeff, N. B., Kelarek, B., Bonar, K., & Stenzel, J. 2017, *PASP*, 129, 054504
- Lafrasse, S., Mella, G., Bonneau, D., et al. 2010, in Proc. SPIE, Vol. 7734, Optical and Infrared Interferometry II, 77344E
- Lanz, T., & Hubeny, I. 2003, *ApJS*, 146, 417
- . 2007, *ApJS*, 169, 83
- Luri, X., Brown, A. G. A., Sarro, L. M., et al. 2018, *A&A*, 616, A9
- Lyubimkov, L. S., Rachkovskaya, T. M., Rostopchin, S. I., & Lambert, D. L. 2002, *MNRAS*, 333, 9
- Lyubimkov, L. S., Rostopchin, S. I., & Lambert, D. L. 2004, *MNRAS*, 351, 745
- Maestro, V., Kok, Y., Huber, D., et al. 2012, in Proc. SPIE, Vol. 8445, Optical and Infrared Interferometry III, 84450G
- Maestro, V., Che, X., Huber, D., et al. 2013, *MNRAS*, 434, 1321
- Ma  z Apell  niz, J., Alfaro, E. J., & Sota, A. 2008, ArXiv e-prints, arXiv:0804.2553
- Ma  z Apell  niz, J., & Barb  , R. H. 2018, *A&A*, 613, A9
- Ma  z Apell  niz, J., Evans, C. J., Barb  , R. H., et al. 2014, *A&A*, 564, A63
- Marcolino, W. L. F., Bouret, J.-C., Martins, F., et al. 2009, *A&A*, 498, 837
- Markova, N., Puls, J., Repolust, T., & Markov, H. 2004, *A&A*, 413, 693
- Martins, F., Escolano, C., Wade, G. A., et al. 2012, *A&A*, 538, A29
- Martins, F., & Plez, B. 2006, *A&A*, 457, 637
- Martins, F., Schaerer, D., & Hillier, D. J. 2005, *A&A*, 436, 1049
- Martins, F., Sim  n-D  az, S., Barb  , R. H., Gamen, R. C., & Ekstr  m, S. 2017, *A&A*, 599, A30

- Martins, F., Hervé, A., Bouret, J.-C., et al. 2015, *A&A*, 575, A34
- Massa, D., & Fitzpatrick, E. L. 2000, *ApJS*, 126, 517
- Massa, D., & Savage, B. D. 1985, *ApJ*, 299, 905
- Megier, A., Strobel, A., Galazutdinov, G. A., & Krełowski, J. 2009, *A&A*, 507, 833
- Mokiem, M. R., de Koter, A., Puls, J., et al. 2005, *A&A*, 441, 711
- Najarro, F., Hanson, M. M., & Puls, J. 2011, *A&A*, 535, A32
- Pasinetti Fracassini, L. E., Pastori, L., Covino, S., & Pozzi, A. 2001, *A&A*, 367, 521
- Poeckert, R., Bastien, P., & Landstreet, J. D. 1979, *AJ*, 84, 812
- Puls, J., Markova, N., Scuderi, S., et al. 2006, *A&A*, 454, 625
- Puls, J., Urbaneja, M. A., Venero, R., et al. 2005, *A&A*, 435, 669
- Repolust, T., Puls, J., Hanson, M. M., Kudritzki, R.-P., & Mokiem, M. R. 2005, *A&A*, 440, 261
- Repolust, T., Puls, J., & Herrero, A. 2004, *A&A*, 415, 349
- Santolaya-Rey, A. E., Puls, J., & Herrero, A. 1997, *A&A*, 323, 488
- Savage, B. D., Bohlin, R. C., Drake, J. F., & Budich, W. 1977, *ApJ*, 216, 291
- Shull, J. M., & van Steenberg, M. E. 1985, *ApJ*, 294, 599
- Simón-Díaz, S., & Herrero, A. 2014, *A&A*, 562, A135
- Simón-Díaz, S., Herrero, A., Esteban, C., & Najarro, F. 2006, *A&A*, 448, 351
- Simón-Díaz, S., Herrero, A., Sabín-Sanjulián, C., et al. 2014, *A&A*, 570, L6
- Sota, A., Maíz Apellániz, J., Walborn, N. R., et al. 2011, *ApJS*, 193, 24
- Swihart, S. J., Garcia, E. V., Stassun, K. G., et al. 2017, *AJ*, 153, 16
- ten Brummelaar, T. A., McAlister, H. A., Ridgway, S. T., et al. 2005, *ApJ*, 628, 453
- Torres, G., Andersen, J., & Giménez, A. 2010, *A&A Rv*, 18, 67
- Turner, N. H., ten Brummelaar, T. A., Roberts, L. C., et al. 2008, *AJ*, 136, 554
- Underhill, A. B., Divan, L., Prevot-Burnichon, M.-L., & Doazan, V. 1979, *MNRAS*, 189, 601
- van Leeuwen, F. 2007, *A&A*, 474, 653